

64

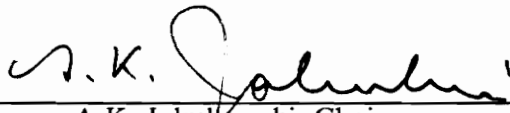
**Approximate Heat-Transfer and Wall-Temperature Calculations
for Aeroassisted Orbital Transfer Vehicles**

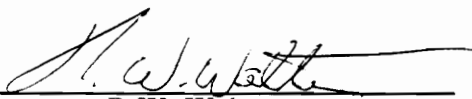
by

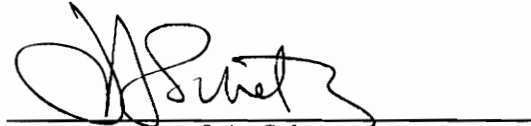
Samir M. Deshpande

Thesis submitted to the Faculty of the
Virginia Polytechnic Institute and State University
in partial fulfillment of the requirements for the degree of
Master of Science
in
Aerospace & Ocean Engineering

APPROVED:


A.K. Jakubowski, Chairman


R.W. Walters


J.A. Schetz

Feb 1988

Blacksburg, Virginia

2

LD
5655
V855
1988
D485
C.2

**Approximate Heat-Transfer and Wall-Temperature Calculations
for Aeroassisted Orbital Transfer Vehicles**

by

Samir M. Deshpande

A.K. Jakubowski, Chairman

Aerospace & Ocean Engineering

(ABSTRACT)

The present work addresses the development of a method for the calculation of Convective heat-transfer and surface temperatures on heat-shields of Aeroassisted Orbital Transfer Vehicles (AOTVs) in hypersonic flow regimes.

Inviscid flowfield solutions are obtained about the aerobraking shield on the AOTVs using axisymmetric Euler's equations. The flowfield solutions are coupled with laminar and turbulent boundary-layer equations and the heat-shield material properties to obtain convective heating rates and heat-shield wall temperatures.

A method for obtaining non-dimensionalized solution of convective heat-transfer rates is obtained. This non-dimensionalized solution can be used for calculating convective heat-transfer rates and wall temperatures for various freestream conditions encountered during the aerobraking maneuvers.

Calculations are carried out for perfect gas and equilibrium air cases, and the effect of wall catalysis on convective heat-transfer is also incorporated. The results are in good agreement with available experimental and numerical results for AOTVs.

Acknowledgments

I am indebted to Dr. A.K. Jakubowski for the help and guidance he has given me throughout this work. Thanks are also due to Dr. R.W. Walters for helping me with all computational work. I wish to thank Dr. J.A. Schetz for serving on my committee.

I take this opportunity to thank all my friends for their help and advice.

This thesis is dedicated to my loving parents.

TABLE OF CONTENTS

Chapter 1. Introduction	1
Chapter 2. Flowfield solution	6
2.1: Governing equations	6
2.2: Finite volume scheme	11
2.3: Equilibrium air calculations	15
Chapter 3. Heat Transfer and Temperature Calculations	16
3.1: Overview	16
3.2: Laminar Heating Equations	17
3.3: Turbulent Heating Equations	20
3.4: Energy balance and Heatshield modelling	22
3.5: Linearization of Energy Balance Equations	25
3.6: Coupling Heat-Transfer and Temperature Equations	27
3.7: Non-Dimensionalization of Heat-Transfer Results	28
Chapter 4. Results and Discussions	30
4.1: Overview	30
4.2: Numerical Results	30

Chapter 5. Conclusions	34
5.1: Overview	34
5.2: Suggestions for future work	35
List of References	36
Tables	39
Figures	42
Vita	87

LIST OF FIGURES

Fig.	Title
1	Thermal Protection System
2	Spherical Cone Aerobrake Configuration
3	EBROEC Aerobrake Configuration
4	Notation for cell (j,k)
5	Heat conduction model with energy balance
6	Computational grid for spherical cone
7	Boundary layer edge pressure distribution $M_\infty = 20$ (perfect gas)
8	Boundary layer edge temperature distribution $M_\infty = 20$ (perfect gas)
9	Boundary layer edge density distribution $M_\infty = 20$ (perfect gas)
10	Boundary layer edge pressure distribution $M_\infty = 25$ (perfect gas)
11	Boundary layer edge temperature distribution $M_\infty = 25$ (perfect gas)
12	Boundary layer edge density distribution $M_\infty = 25$ (perfect gas)
13	Boundary layer edge pressure distribution $M_\infty = 30$ (perfect gas)
14	Boundary layer edge temperature distribution $M_\infty = 30$ (perfect gas)
15	Boundary layer edge density distribution $M_\infty = 30$ (perfect gas)
16	Variation of heat transfer with altitude
17	Variation of heat transfer with ρ_∞
18	Variation of heat transfer with T_∞
19	Variation of heat transfer with Mach number
20	Wall temperatures $M_\infty = 20$, $H = 280$ kft (perfect gas)
21	Wall temperatures $M_\infty = 25$, $H = 280$ kft (perfect gas)

22	Wall temperatures $M_\infty = 30$, $H = 280$ kft (perfect gas)
23	Variation of inside temperature with insulation thickness
24	Variation of surface temperature with altitude
25	Comparison of Laminar and Turbulent heating rates
26	Non-dimensional heat transfer for spherical cone
27	Boundary layer edge pressure distribution $M_\infty = 20$ (eq. air)
28	Boundary layer edge Temperature distribution $M_\infty = 20$ (eq. air)
29	Boundary layer edge density distribution $M_\infty = 20$ (eq. air)
30	Comparison of perfect gas and eq. air heating rates
31	Wall temperatures $M_\infty = 20$ (eq. air)
32	Heat transfer $M_\infty = 20$, $H = 220$ kft (non-catalytic)
33	Wall temperatures $M_\infty = 20$, $H = 220$ kft (non-catalytic)
34	Computational grid for EBROEC
35	Boundary layer edge pressure distribution $M_\infty = 20$ (perfect gas)
36	Boundary layer edge temperature distribution $M_\infty = 20$ (perfect gas)
37	Boundary layer edge density distribution $M_\infty = 20$ (perfect gas)
38	Heat transfer $M_\infty = 20$, $H = 280$ kft (perfect gas)
39	Wall temperatures $M_\infty = 20$, $H = 280$ kft (perfect gas)
40	Comparison of calculated and experimental results for Sp. Cones
41	Comparison of calculated results with other methods for Sp. Cones
42	Comparison of calculated and experimental results for EBROEC
43	Comparison of calculated results with other methods for EBROEC
44	Pressure distribution predicted by modified Newtonian theory
45	Heating rates for Newtonian theory with Thwaites-Walz method

NOMENCLATURE

a	Sound speed
C_f	Skin-friction coefficient
C_p	Specific heat at constant pressure
e	Energy (per unit volume)
e_o	Internal energy (per unit mass)
h	Heat transfer coefficient
H	Enthalpy, Altitude
H_c	Form factor
k	Thermal conductivity
L	Characteristic length
M	Mach number
N	Reciprocal exponent in power law
p	Pressure
Pr	Prandtl number
\dot{q}	Heat-transfer rate
\bar{r}	Recovery factor
R_N	Nose radius
R_θ	Momentum thickness Reynolds number
s	Distance along surface from stag. pt.
St	Stanton number
T	Temperature
V_∞	Free-stream velocity

γ	Ratio of specific heats
ε_0	Surface emissivity
θ	Momentum thickness
μ	Dynamic viscosity
ρ	Density
σ	Boltzmann constant
ω	Relaxation factor

Subscripts and Superscripts

aw	Adiabatic wall
c	Convective-heating rate
e	boundary layer edge
L	Laminar
r	Radiative-heating rate
s	Stagnation point
T	Turbulent
w	Wall
$*$	Reference conditions
∞	Free-stream conditions

Chapter 1. Introduction

The possibility of using aerodynamic forces for orbital plane changes was first proposed by Howard London [1]. This method could produce orbital plane changes with a much smaller expenditure of energy compared to the extra-atmospheric all-propulsive maneuver. This would result in a lower requirement of propellant fuel, and thus increased payload capabilities. The potential for the use of this method in planetary capture for manned missions to Mars was shown in 1964. For planetary capture, the aerodynamic forces mainly used are the drag forces to reduce the vehicle velocity. The lift forces are used only for minor trajectory corrections. Such a maneuver is called Aeroassisted orbital transfer, or aerobraking. Studies have been carried out for the use of aerobraking in orbital transfer from GEO to LEO. The present focus is on the use of Aeroassisted Orbital Transfer Vehicles (AOTVs) for Lunar and planetary missions, either manned or unmanned.

The AOTV configurations require an aerobraking shield in the front of the vehicle. Some of the configurations proposed for the aerobraking shields are blunted spherical cones, lifting ballutes and ellipsoidally blunted raked-off elliptic cones (EBROEC). All these

configurations have very low L/D ratios to fulfill the requirement of a high drag coefficient. These configurations have very high heating rates near stagnation region and corners. The structural integrity of the vehicle and the aerobraking shield require temperatures within acceptable limits. This necessitates the use of a Thermal Protection System (TPS) on the aerobraking shield (fig. 1). The TPS consists of surface insulation which protects the vehicle and the primary structure of the aerobrake from effects of the aerothermal environment.

For the design of TPS, it is necessary to calculate heating-rates and the temperatures on the front and back sides of TPS. Various methods can be used for the calculation of heat-transfer rates to the TPS. The easiest method for such a calculation is the Engineering Correlation (EC) formula [3], which gives a rough estimate of the heating rates for the nose region of a blunt reentry body. The heating rate \dot{q} to the stagnation point (nose radius R_N) is given as a function of freestream conditions by the following equation

$$\dot{q} = 18300 \rho_{\infty}^{0.5} (V_{\infty}/10^4)^{3.05} R_N^{-0.5} \quad (W/cm^2)$$

where ρ_{∞} is the free stream density and V_{∞} is the free stream velocity. This formula tends to provide a conservative approximation of the heating rate. However, this approximation can not be used for design studies to determine the configuration of the aerobraking shield as it only takes the nose radius into consideration for the calculation of the stagnation point heating rate \dot{q} and does not provide any information regarding the distribution of the heating rate on the body. With this approach, the stagnation heat fluxes depend only on the nose radius and are independent of the aerobrake diameter.

Results may be valid for configurations where the sonic line remains on the spherical nose, however, they tend to be on the higher side for most of the AOTV aerobrake shapes of practical interest. For locations other than stagnation point, the heat flux distribution may be obtained by using surface pressure distributions derived from modified Newtonian theory and simple boundary layer analysis like the Thwaites-Walz method. This might seem to be accurate enough for a preliminary analysis, however, for bodies with flat regions, the results obtained vary considerably from a detailed analysis due to a zero pressure gradient on the flat region. As most of the aeroassist vehicles of interest have large conical areas, this method is not applicable. Other methods use viscous shock-layer solutions, Navier-Stokes solutions etc.. These methods provide very accurate heat-transfer rates, but require high mesh resolution near the wall and large computational times. This makes them economically non-feasible for design studies, and they are used only for detailed calculations once the configuration has been decided.

The present study concentrates on the development of a reasonably accurate method to be used for the calculation of convective heat-transfer rates and TPS wall temperatures in design studies. The convective heating-rates and wall-temperatures can be calculated by this method for axisymmetric bodies at zero angle of attack. This method can also be used for 3-Dimensional bodies, or bodies with non-zero angle of attack by using the axisymmetric analogue. The axisymmetric analogue uses a corresponding axisymmetric body for approximating flow over some part of a 3-D flow problem. First the inviscid solution is obtained using the axisymmetric Euler's equations for either perfect gas or equilibrium air. The surface values of stream velocity, temperature, density and pressure are taken from the inviscid solution and coupled with approximate convective heating rate equations and equations modelling the energy balance on the TPS walls. The method chosen for boundary layer calculations has the advantage that inspite of

simplification of the equations, it gives very good results for compressible boundary layers. The values of heat-transfer and temperatures are calculated by an iterative procedure.

Finally, the results are used for the development of a method for non-dimensionalizing the heat-transfer results. The freestream properties M_∞ , ρ_∞ and T_∞ are used as the non-dimensionalization parameters. This collapses the data for convective heat-transfer rates to the aerobraking shield wall. The advantage of such a non-dimensionalization is that heat-transfer and wall temperatures can be calculated for various reentry conditions, once a solution has been obtained for a particular body under a certain set of conditions. The calculations for a different set of conditions then do not require the solution of inviscid flowfield for varying Mach number. This results in the saving of considerable amount of computational time required for design studies.

For a given aerobrake configuration, significant reductions in convective heating may be obtained by selecting appropriate materials and coatings having low catalytic efficiency with regard to the recombination of atomic oxygen and nitrogen. Such reductions have been predicted by calculations based on the non-equilibrium chemistry Boundary Layer Integral Matrix Procedure [19] and were suggested by STS-2 reentry heating data. For the purpose of preliminary design studies, the effect of surface catalysis may be accounted for by application of a catalysis factor selected according to materials and coatings of the TPS.

The magnitude of the radiative contribution to the heat transfer can not be, at present, predicted accurately. Most analysis of radiation have been based on the assumption that the gas is in chemical equilibrium; the gas radiation contribution is then small compared to the convection term. However, some investigations [22] have shown that for the initial

OTV heating conditions, the flow gas chemistry in the stagnation region will significantly deviate from the equilibrium state and this may lead to radiative heating of the same order as the convective values. According to other investigations [4], both equilibrium and non-equilibrium gas radiation heating will be less than about 10 percent of the convection heating. Current estimates of stagnation point radiation intensity vary widely and no established guidelines are available to account for velocity, altitude and location on the aerobrake. To resolve this controversy and the different interpretations of the available non-equilibrium radiative heating data, NASA plans to carry out a series of aeroassisted flight experiments by using a free-flying, shuttle-launched and recovered spacecraft (current launch date is Sept. 1991).

Chapter 2. Flowfield Solution

2.1 Governing Equations

The axisymmetric Euler's equations are used for calculation of the inviscid flowfield. The four equations are conservation of mass, x-momentum, r-momentum and energy equations. These equations have been solved for perfect-gas and equilibrium-air conditions. The conservation form of the equations is given by

$$\frac{\partial Q}{\partial t} + \frac{\partial F}{\partial x} + \frac{\partial G}{\partial r} = P \quad (2.1.1)$$

where

$$Q = \begin{bmatrix} \rho r \\ \rho u r \\ \rho v r \\ e r \end{bmatrix} \quad (2.1.2)$$

$$F = \begin{bmatrix} \rho u r \\ (\rho u^2 + p)r \\ \rho u v r \\ (e + p)u r \end{bmatrix} \quad (2.1.3)$$

$$G = \begin{bmatrix} \rho v r \\ \rho u v r \\ (\rho v^2 + p)r \\ (e + p)v r \end{bmatrix} \quad (2.1.4)$$

$$P = \begin{bmatrix} 0 \\ 0 \\ p \\ 0 \end{bmatrix} \quad (2.1.5)$$

These equations are non-dimensionalized in terms of the freestream properties. The non-dimensional quantities are given as

$$\rho = \frac{\rho'}{\rho'_{\infty}} \quad (2.1.6)$$

$$u = \frac{u'}{V'_\infty} \quad (2.1.7)$$

$$v = \frac{v'}{V'_\infty} \quad (2.1.8)$$

$$e = \frac{e'}{\rho'_\infty V'^2_\infty} \quad (2.1.9)$$

$$p = \frac{p'}{\rho'_\infty V'^2_\infty} \quad (2.1.10)$$

$$T = \frac{T'}{T'_\infty} \quad (2.1.11)$$

The prime denotes dimensional quantities. These non-dimensionalizing parameters are chosen such that the non-dimensionalized equations have the same form as the dimensional equations. The equation of state is required to complete the set of equations. Non-dimensional equation of state for perfect gas is given by

$$p = \frac{\rho T}{\gamma M^2_\infty} \quad (2.1.12)$$

and the pressure can then be written in terms of the conserved variables as

$$p = (\gamma - 1) \left[e - \rho \frac{u^2 + v^2}{2} \right] \quad (2.1.13)$$

Equation 2.1.1 can be transformed into generalized coordinates ξ and η . The generalized coordinates are chosen such that they correspond to the computational grid.

The equation in the generalized form is written as

$$\frac{\partial \hat{Q}}{\partial t} + \frac{\partial \hat{F}}{\partial \xi} + \frac{\partial \hat{G}}{\partial \eta} = \hat{P} \quad (2.1.14)$$

where

$$\hat{Q} = \frac{1}{J} \begin{bmatrix} \rho r \\ \rho u r \\ \rho v r \\ e r \end{bmatrix} \quad (2.1.15)$$

$$\hat{F} = \frac{1}{J} \begin{bmatrix} \rho U r \\ (\rho U u + \xi_x p) r \\ (\rho U v + \xi_r p) r \\ (e + p) U r \end{bmatrix} \quad (2.1.16)$$

$$\hat{G} = \frac{1}{J} \begin{bmatrix} \rho V r \\ (\rho V u + \eta_x p) r \\ (\rho V v + \eta_r p) r \\ (e + p) V r \end{bmatrix} \quad (2.1.17)$$

$$\hat{P} = \frac{1}{J} \begin{bmatrix} 0 \\ 0 \\ p \\ 0 \end{bmatrix} \quad (2.1.18)$$

where J is the jacobian of transformation given by

$$J = \begin{vmatrix} \xi_x & \xi_r \\ \eta_x & \eta_r \end{vmatrix} \quad (2.1.19)$$

where ξ and η are of the form

$$\xi = \xi(x, r) \quad (2.1.20)$$

$$\eta = \eta(x, r) \quad (2.1.21)$$

The contravariant velocity components are given by

$$U = \xi_x u + \xi_r v \quad (2.1.22)$$

$$V = \eta_x u + \eta_r v \quad (2.1.23)$$

These equations are solved by using a finite volume formulation.

2.2 Finite Volume Scheme

The flowfield around the AOTV is hypersonic and the steady solution has a strong shock wave. Upwind methods provide a means for the computation of the solution for such flows. This results from a direct simulation of the signal-propagation features of hyperbolic equations by these methods. Moreover, these methods are naturally dissipative and hence no artificial viscosity terms are required [5].

The implicit upwind method with flux-vector splitting is used for the present calculations. The flux-splitting scheme used has been developed by Van Leer [6]. A relaxation algorithm has been used as given by Thomas, Van Leer and Walters [8]. The first order fully upwind differencing is used for all the calculations.

The Van Leer flux-splitting has an advantage that it is continuously differentiable through eigen-value sign changes which occur at stagnation points and sonic points. The flux-splitting for the fluxes \hat{F} and \hat{G} is given as

$$\hat{F}^{\pm} = \frac{grad(\xi)}{J} \begin{bmatrix} f_{mass}^{\pm} \\ f_{mass}^{\pm} [\hat{k}_x (-\bar{u} \pm 2a)/\gamma + u] \\ f_{mass}^{\pm} [\hat{k}_r (-\bar{u} \pm 2a)/\gamma + v] \\ f_{energy}^{\pm} \end{bmatrix} \quad (2.2.1)$$

where

$$\bar{u} = \frac{U}{grad(\xi)} \quad (2.2.2)$$

$$M_{\xi} = \frac{\bar{u}}{a} \quad (2.2.3)$$

$$f_{mass}^{\pm} = \frac{\pm \rho a (M_{\xi} \pm 1)^2 r}{4} \quad (2.2.4)$$

$$f_{energy}^{\pm} = f_{mass}^{\pm} \left\{ \frac{[-(\gamma - 1)\bar{u}^2 \pm 2(\gamma - 1)\bar{u}a + 2a^2]}{(\gamma^2 - 1)} + \frac{(u^2 + v^2)}{2} \right\} \quad (2.2.5)$$

$$\hat{k}_x = \frac{\xi_x}{grad(\xi)} \quad (2.2.6)$$

$$\hat{k}_r = \frac{\xi_r}{grad(\xi)} \quad (2.2.7)$$

similarly for the flux G , the splitting is carried out as

$$\hat{G}^{\pm} = \frac{grad(\eta)}{J} \begin{bmatrix} g_{mass}^{\pm} \\ g_{mass}^{\pm} [\hat{l}_x (-\bar{v} \pm 2a)/\gamma + u] \\ g_{mass}^{\pm} [\hat{l}_r (-\bar{v} \pm 2a)/\gamma + v] \\ g_{energy}^{\pm} \end{bmatrix} \quad (2.2.8)$$

where

$$\bar{v} = \frac{V}{grad(\eta)} \quad (2.2.9)$$

$$M_{\eta} = \frac{\bar{v}}{a} \quad (2.2.10)$$

$$g_{mass}^{\pm} = \frac{\pm \rho a (M_{\eta} \pm 1)^2 r}{4} \quad (2.2.11)$$

$$g_{energy}^{\pm} = g_{mass}^{\pm} \left\{ \frac{[-(\gamma - 1)\bar{v}^2 \pm 2(\gamma - 1)\bar{v}a + 2a^2]}{(\gamma^2 - 1)} + \frac{(u^2 + v^2)}{2} \right\} \quad (2.2.12)$$

$$\hat{l}_x = \frac{\eta_x}{grad(\eta)} \quad (2.2.13)$$

$$\hat{l}_r = \frac{\eta_r}{grad(\eta)} \quad (2.2.14)$$

The relaxation algorithm is implemented with a backward-time implicit integration scheme. Equation (2.1.14) is written in the form:

$$\frac{\partial \hat{Q}}{\partial t} - R^{n+1} = 0 \quad (2.2.15)$$

where

$$R^{n+1} = - \left[\frac{\partial \hat{F}}{\partial \xi} + \frac{\partial \hat{G}}{\partial \eta} - \hat{P} \right]^{n+1} \quad (2.2.16)$$

Taking backward-time difference

$$\frac{\Delta \hat{Q}}{\Delta t} = R^{n+1} = R^n + \Delta R \quad (2.2.17)$$

where

$$\Delta \hat{Q} = \hat{Q}^{n+1} - \hat{Q}^n \quad (2.2.18)$$

$$\Delta R \simeq \frac{\partial R}{\partial \hat{Q}} \Delta \hat{Q} \quad (2.2.19)$$

This results in the following equation:

$$\left[\frac{I}{\Delta t} - \frac{\partial R}{\partial \hat{Q}} \right] \Delta \hat{Q} = R^n \quad (2.2.20)$$

For first order accurate solution using vertical line Gauss-Seidel scheme, the equation can be written in the form:

$$a \Delta \hat{Q}_{j, k-1} + b \Delta \hat{Q}_{j, k} + c \Delta \hat{Q}_{j, k+1} = R^n - d \Delta \hat{Q}_{j-1, k} \quad (2.2.21)$$

This is solved by sweeping along j direction . a, b and c are 4×4 blocks, which are functions of $\frac{\partial \hat{F}}{\partial \hat{Q}}$ and $\frac{\partial \hat{G}}{\partial \hat{Q}}$.

The boundary conditions taken are as follows : freestream at $K = KMAX$; symmetry condition at $J=1$; tangency to the wall at $K = 1$; and supersonic outflow at $J = JMAX$. The cell (j,k) is shown in fig. 1.

2.3 Equilibrium Air Calculations

The equilibrium air calculations are carried out by using the same equations as the perfect gas calculations. However, the effects of dissociation and ionization are incorporated by using a method for equilibrium air developed by Grossman and Walters [9]. This method uses an equivalent $\bar{\gamma}$ in the place of γ which is calculated from equilibrium air routines. $\bar{\gamma}$ is defined by the following equation

$$\bar{\gamma} = 1 + \frac{p}{\rho e_o} \quad (2.3.1)$$

where p , ρ and e_o are dimensional quantities. e_o is the internal energy per unit mass.

Chapter 3. Heat Transfer and Temperature Calculations

3.1 Overview

The non-dimensionalized flowfield solution obtained from the axisymmetric Euler equations is used as the edge conditions for the boundary layer. There are many existing methods that use the inviscid flowfield solution for the heat-transfer calculations. Notable amongst these is the method of Cohen [10] and the method of Sutton and Graves [11]. Cohen's equation is used for air calculations and is given as

$$\dot{q}_{w,s} = 0.767 Pr_w^{-0.6} (H_s - H_w) (\rho\mu)_{w,s}^{0.07} \left(\frac{du}{ds}\right)_{e,s}^{0.5} \quad (3.1.1)$$

Equation of Sutton and Graves is given as

$$\dot{q}_{w,s} = K \left(\frac{\rho_s}{R_N} \right)^{0.5} (H_s - H_w) \quad (3.1.2)$$

where K can be determined for a variety of gas mixtures. Both these methods are in good agreement with available experimental data. However, only stagnation point calculations can be carried out by these methods. For the calculation of laminar and boundary layer heat-transfer distributions along the surface, the method of Zoby, Moss and Sutton [12] produces good results. This method has been used in the prediction of convective heating rates.

3.2 Laminar Heating Equations

The laminar heat-transfer distributions are computed by relating the convective heat transfer to a skin-friction relation based on the momentum-thickness Reynolds number R_θ through a modified Reynolds analogy form. The laminar heat transfer is computed using the incompressible Blasius [14] relations and Eckert's reference enthalpy relation. The skin friction relation is given as

$$C_f = \frac{(0.664)^2}{R_\theta} \quad (3.2.1)$$

Eckert's reference enthalpy relation is given as

$$H^* = H_e + 0.5(H_w - H_e) + 0.22(H_{aw} - H_e) \quad (3.2.2)$$

where

$$H_{aw} = H_e + \bar{r} \frac{u_e^2}{2} \quad (3.2.3)$$

\bar{r} is the recovery factor. The value of \bar{r} can be approximated by the following equation for a variety of conditions

$$\bar{r} = \sqrt{Pr} \quad (3.2.4)$$

These are used in the following equations

$$\dot{q}_{c,L} = h(H_{aw} - H_w) \quad (3.2.5)$$

$$h = \rho^* u_e St^* \quad (3.2.6)$$

$$St^* = \frac{C_f}{2} (Pr_w)^{-0.6} \quad (3.2.7)$$

The resulting laminar heat-transfer equation is

$$\dot{q}_{c,L} = 0.22 (R_{\theta,e})^{-1} \left(\frac{\rho}{\rho_e}\right)^* \left(\frac{\mu}{\mu_e}\right)^* \rho_e u_e (H_{aw} - H_w) (Pr_w)^{-0.6} \quad (3.2.8)$$

where θ_L is obtained by integrating the axisymmetric boundary layer equation

$$\frac{d\theta}{ds} + \theta \left[\frac{1}{u_e} \frac{du_e}{ds} (2 + H_c) + \frac{1}{r} \frac{dr}{ds} + \frac{1}{\rho_e} \frac{d\rho_e}{ds} \right] = \frac{\tau_o}{\rho_e u_e^2} \quad (3.2.9)$$

$$\theta_L = 0.664 \frac{\left(\int_0^s \rho^* \mu^* u_e r^2 ds \right)^{0.5}}{(\rho_e u_e r)} \quad (3.2.10)$$

where s is the distance along the surface and r is the radius of the body of revolution at the cross-section of interest.

For perfect gas calculations, the quantities ρ^* , μ^* are calculated at the reference temperature T^* given by

$$T^* = T_e + 0.5(T_w - T_e) + 0.22(T_{aw} - T_e) \quad (3.2.11)$$

The enthalpy H_{aw} and H_w are calculated by

$$H_{aw} = C_p T_{aw} \quad (3.2.12)$$

$$H_w = C_p T_w \quad (3.2.13)$$

where T_{aw} is the adiabatic wall temperature value calculated from the flowfield edge conditions. T_{aw} is given by

$$T_{aw} = T_e + \bar{r} \frac{u_e^2}{2C_p} \quad (3.2.14)$$

The dynamic viscosity is calculated by using Sutherland formula

$$\mu = 0.1716 \left(\frac{T}{273.1} \right)^{1.5} \frac{383.7 \times 10^{-4}}{(T + 110.6)} \quad (3.2.15)$$

where T is in degree Kelvin and μ is in Ns/m^2

For equilibrium air calculations, the reference quantities ρ^* , μ^* are calculated at the reference temperature T^* which corresponds to the reference enthalpy H^* . T^* is calculated from H^* by the use of equilibrium air routines.

3.3 Turbulent Heating Equations

Similar to the laminar heating-rate calculations, the turbulent heat transfer is also computed by a skin-friction relation based on R_θ . Most of the turbulent boundary layer calculations assume a 1/7 th velocity profile. However, experimental results have shown that the value of N in 1/N velocity profile varies from 7 for very high values R_θ to 4 for R_θ below 1000. A compressible turbulent analysis has demonstrated the effect of variable N on the skin-friction. Zoby, Moss and Sutton give the following relation for the skin-friction coefficient

$$C_f = 2C_1(R_{\theta,e})^{-m} \quad (3.3.1)$$

This is substituted into the momentum equation to yield the expression for turbulent momentum thickness as

$$\theta_T = \frac{C_2 \left(\int_0^s \rho^* \mu^{*m} u_e r^{c_3} ds \right)^{c_4}}{(\rho_e u_e r)} \quad (3.3.2)$$

where the constants m, c_1, c_2, c_3, c_4 are functions of N . These constants are defined by the following relations:

$$m = \frac{2}{N+1} \quad (3.3.3)$$

$$C_1 = \left(\frac{1}{C_5} \right)^{\frac{2N}{N+1}} \left[\frac{N}{(N+1)(N+2)} \right]^m \quad (3.3.4)$$

$$C_2 = (1+m)C_1 \quad (3.3.5)$$

$$C_3 = 1+m \quad (3.3.6)$$

$$C_4 = \frac{1}{C_3} \quad (3.3.7)$$

$$C_5 = 2.2433 + 0.94 N \quad (3.3.8)$$

Using the skin friction form in equation (3.3.1) we get the following equation for the turbulent heat-transfer

$$\dot{q}_{c,T} = C_1 (R_{\theta,e})^{-m} \left(\frac{\rho}{\rho_e}\right)^* \left(\frac{\mu}{\mu_e}\right)^* \rho_e u_e (H_{aw} - H_w) (Pr_w)^{-0.4} \quad (3.3.9)$$

For the calculation of the value of N, it is necessary to guess a starting value of N to calculate the constants m , C_1 , C_2 , C_3 and C_4 . These constants are used to calculate the momentum thickness θ_T by using equation (3.3.2). Finally the corresponding value of $R_{\theta,e}$ is used to calculate N by the following curve fit of axisymmetric wall data

$$N = 12.67 - 6.51 \log(R_{\theta,e}) + 1.21[\log(R_{\theta,e})]^2 \quad (3.3.10)$$

The iteration process is carried out until a converged solution for N is obtained. However it should be noted that the curve fit is good for values of R_{θ} higher than approximately 500, and thus N has been taken as 3.9 for all values of R_{θ} less than 500.

The reference quantities T^* , ρ^* and μ^* are calculated as explained in the laminar heating rate calculations.

3.4 Energy Balance and Heatshield Modelling

The temperatures on the outer surface of the TPS and on the structure inside the TPS are calculated by carrying out a quasi-static energy balance. The aerobrake typically has a supporting structure with TPS tiles or other insulating materials on the outer surface. Thus, in the simplest case, the TPS and the structure may be modelled as a two layer system. A one-dimensional heat-transfer model is assumed with surface radiation from

the TPS material and the leeward side of the structure. A non-ablating surface has been assumed.

The energy balance requires that the total convective heat-flux to the surface equals the re-radiative heat-flux from the heatshield. It is assumed that convective heat-transfer takes place only on the forward surface of the aerobrake (fig. 2). This gives the following equation

$$\dot{q}_c - \dot{q}_{r_1} - \dot{q}_{r_2} = 0 \quad (3.4.1)$$

where the subscripts 1 and 2 refer to the windward and leeward surfaces of the aerobrake respectively.

The 1-D heat-transfer through the wall is given by

$$\dot{q}_{r_2} = k_1 \frac{T_1 - T_3}{x_1} = k_2 \frac{T_3 - T_2}{x_2}$$

this gives a relation for the two surface temperatures as

$$T_1 - T_2 = \dot{q}_{r_2} \left(\frac{x_1}{k_1} + \frac{x_2}{k_2} \right) \quad (3.4.2)$$

using the Stefan-Boltzmann law, the radiative fluxes are related to the surface temperature as

$$\dot{q}_{r_1} = \varepsilon_{o_1} \sigma T_1^4 \quad (3.4.3)$$

$$\dot{q}_{r_2} = \varepsilon_{o_2} \sigma T_2^4 \quad (3.4.4)$$

For materials which have the conductivity k varying as a function of temperature, the following equations are used

$$k_1 = f_1(\bar{T}_1) \quad (3.4.5)$$

$$k_2 = f_2(\bar{T}_2) \quad (3.4.6)$$

where f_1 and f_2 are given functions for the heatshield materials. \bar{T}_1 and \bar{T}_2 are average temperature values given by

$$\bar{T}_1 = 0.5 \left[2T_1 - \dot{q}_{r_2} \frac{x_1}{k_1} \right] \quad (3.4.7)$$

$$\bar{T}_2 = 0.5 \left[T_1 + T_2 - \dot{q}_{r_2} \frac{x_1}{k_1} \right] \quad (3.4.8)$$

The values of k are calculated by taking the temperature, conductivity and heating-rate values from the previous iteration step. This keeps the number of simultaneous equations to be solved at 4.

3.5 Linearization of Energy Balance Equations

The four equations governing energy balance (equations 3.4.1 to 3.4.4) are solved by Newton's method. This requires the linearization of the equations. The equations can be rewritten as

$$f(1) = \dot{q}_{r_1} + \dot{q}_{r_2} - \dot{q}_c \quad (3.5.1)$$

$$f(2) = \left[\frac{x_1}{k_1} + \frac{x_2}{k_2} \right] \dot{q}_{r_2} - T_1 + T_2 \quad (3.5.2)$$

$$f(3) = \dot{q}_{r_1} - \varepsilon_{o_1} \sigma T_1^4 \quad (3.5.3)$$

$$f(4) = \dot{q}_{r_2} - \varepsilon_{o_2} \sigma T_2^4 \quad (3.5.4)$$

taking the four variables as

$$x(1) = \dot{q}_{r_1} \quad (3.5.5)$$

$$x(2) = \dot{q}_{r_2} \quad (3.5.6)$$

$$x(3) = T_1 \quad (3.5.7)$$

$$x(4) = T_2 \quad (3.5.8)$$

Linearization of this problem gives

$$\left[\frac{\partial f}{\partial x}\right]\{\Delta x\} = \{f(x)\} \quad (3.5.9)$$

where

$$\left[\frac{\partial f}{\partial x}\right] = \begin{bmatrix} 1 & 1 & 0 & 0 \\ 0 & \frac{x_1}{k_1} + \frac{x_2}{k_2} & -1 & 1 \\ 1 & 0 & -4\varepsilon_{o_1}\sigma T_1^3 & 0 \\ 0 & 1 & 0 & -4\varepsilon_{o_2}\sigma T_2^3 \end{bmatrix}$$

The linearized system of equations (3.5.9) is solved by Gauss-Siedel iteration.

The formulation of the problem can be easily modified for any number of layers in the wall. For the generalized case of n layers, equations (3.4.7) and (3.4.8) can be rewritten in the following form

$$\bar{T}_m = T_1 - \dot{q}r_2 \left[\sum_{i=1}^{m-1} \frac{x_i}{k_i} + \frac{x_m}{2k_m} \right] \quad (3.4.7a)$$

$$\frac{\partial f(2)}{\partial x(2)} = \sum_{i=1}^n \frac{x_i}{k_i} \quad (3.4.8a)$$

where

$$k_i = f_i(\bar{T}_i) \quad (3.4.5a)$$

3.6 Coupling the Heat-Transfer and Temperature Equations

In sections 3.2 and 3.3, the heating-rate equations for laminar and turbulent boundary layers have been presented. Both these calculations are based on reference enthalpy. Reference enthalpy is a function of the boundary layer edge conditions and the wall temperature. However, the wall temperature is calculated by energy balance as shown in sections 3.4 and 3.5. This makes it necessary to couple the wall temperature and convective heat-transfer equations.

An iterative method has been used for coupling these equations. The freestream temperature value is used as the starting value of wall temperature. The heating-rate is calculated from the boundary layer edge properties and the wall temperature values. This is in turn used for the calculation of wall temperature values. This iteration scheme is highly divergent in nature if the calculated value of wall temperature is used in the next iteration step. An under relaxation technique is used for correcting this problem and the correct value of wall temperature is calculated by the following equation

$$T^{n+1} = T^n + \omega^n \Delta \tilde{T} \quad (3.6.1)$$

where

$$\Delta \tilde{T} = \tilde{T}^{n+1} - T^n \quad (3.6.2)$$

T^n and T^{n+1} are the values of outer wall temperatures after n and $n+1$ iterations respectively. \tilde{T}^{n+1} is the temperature calculated from the energy balance equations. ω^n is the under-relaxation factor and is given by

$$\omega^n = \frac{0.99}{1 + \Delta\tilde{T}/T^n} \quad (3.6.3)$$

This under-relaxation factor has the effect of reducing $\Delta T/\Delta\tilde{T}$ when $\Delta\tilde{T}$ is large compared to T^n but results in almost no under-relaxation when $\Delta\tilde{T}/T^n$ is very small. The constant factor of 0.99 is seen to prevent an oscillating non-convergent solution.

3.7 Non-Dimensionalization of Heat-Transfer Results

The convective heat-transfer to the surface of the aerobrake is found to depend on the inviscid solution strongly. However, it does not vary much with the wall temperatures. This gives rise to the idea of non-dimensionalizing the heat-transfer results in terms of the freestream properties M_∞ , ρ_∞ and T_∞ . A solution of the following form was sought

$$\dot{q}_c = M_\infty^a \rho_\infty^b T_\infty^c \bar{q}_c \quad (3.7.1)$$

where \bar{q}_c is some non-dimensionalized value of the convective heat-transfer rate. The exponents a , b and c are calculated by getting results of \dot{q}_c for various values of M_∞ , ρ_∞ and T_∞ . This results in a solution of the following form

$$\bar{q}_c = \bar{q}_c(s) \quad (3.7.2)$$

where s is measured along the surface of the aerobrake from the stagnation point.

For the calculation of wall temperature and heating-rate values at any set of freestream conditions, first the heating rate \dot{q}_c is calculated from \bar{q}_c and then this value is used for calculating T_1 and T_2 by using equations (3.4.1) to (3.4.4).

Chapter 4. Results and Discussions

4.1 Overview

Heat transfer and temperature results have been obtained for two types of aerobraking shield configurations. These are spherical cone and ellipsoidally blunted raked off elliptic cone (EBROEC). These calculations were performed, in part, in support of the TAXI project sponsored by NASA/USRA. For the EBROEC, the computations are carried out for the plane perpendicular to the symmetry plane through the stagnation point.

Calculations are carried out for various values of M_∞ and different altitudes. Dependence of the heating rates on the freestream Mach number, temperature and density has been found for perfect gas. Calculations have also been carried out for equilibrium air with fully catalytic and non-catalytic wall cases.

4.2 Numerical Results

The numerical grid for the spherical cone is shown in fig. 6. The grid has 60 points in ξ direction and 40 points in η direction. The grid points are clustered near the wall.

Symmetry condition is prescribed at the lower boundary, tangency condition at the wall, freestream condition at inflow boundary, and supersonic outflow at remaining boundary.

Figs. 7 to 15 show the computational results obtained for pressure, temperature and density at the boundary layer edge at freestream Mach numbers of 20, 25 and 30 for the spherical cone using perfect gas assumption. The pressure, temperature and density values have been non-dimensionalized using the freestream values of those quantities. These are used as the boundary layer edge properties for heat transfer calculations.

The atmospheric encounter for AOTVs takes place typically between the altitudes of 220,000 and 310,000 ft. As the freestream density values are very low at these altitudes, the flow is essentially laminar in nature. Fig. 16 shows the variation of heat transfer with the altitude at the Mach number of 20. Figs. 17, 18 and 19 show the variation of heat transfer with ρ_∞ , T_∞ and M_∞ respectively. This data is used for deciding the non-dimensionalizing coefficients for heat transfer.

Structural materials have limitations on the operating temperatures, and the insulation thickness can be varied to achieve the required value of inside temperature. The insulation material used for the calculations was Flexible Reusable Surface Insulation (FRSI). From the table of properties for this material in reference [21], the following cubic fit can be obtained for the thermal conductivity

$$k = 4.887 \times 10^{-11} T^3 - 4.170 \times 10^{-8} T^2 + 7.949 \times 10^{-5} T + 2.832 \times 10^{-3} \quad (4.2.1)$$

where the temperature is in $^{\circ}k$ and conductivity is in $W/m^{\circ}k$. Using this insulation model, the temperature values for the TPS are calculated. The results for an altitude of

280,000 ft. and free stream mach numbers of 20, 25 and 30 are given in figs. 20 to 22 respectively. Variation of the inside wall temperature with insulation thickness is shown in fig. 23. Fig. 24 shows the variation of the TPS surface temperature with altitude. A comparison of the Turbulent and Laminar heating rates is given in fig. 25.

Heat transfer values at different conditions can be related as follows

$$\frac{\dot{q}_2}{\dot{q}_1} = \left(\frac{M_{\infty 2}}{M_{\infty 1}} \right)^{3.07} \left(\frac{T_{\infty 2}}{T_{\infty 1}} \right)^{1.554} \left(\frac{\rho_{\infty 2}}{\rho_{\infty 1}} \right)^{0.49} \quad (4.2.2)$$

Thus the non-dimensionalized value of the heat transfer is given by

$$\bar{q} = \frac{\dot{q}}{M_{\infty}^{3.07} T_{\infty}^{1.554} \rho_{\infty}^{0.49}} \quad (4.2.3)$$

This is seen to have a form very similar to the Engineering correlation (EC) formula. The non-dimensional \bar{q} values are shown in fig. 26 for the spherical cone.

Figs. 27 to 29 give the flowfield solution at the wall for equilibrium air at $M_{\infty} = 20$ and $H = 220,000$ ft. The comparison of the heating rates for perfect gas and equilibrium air (fully-catalytic wall) is given in fig. 30. This shows that the fully catalytic wall has higher heating rates due to the dumping of heat resulting from recombination of the gas at the wall. Fig. 31 shows the temperature distribution for the equilibrium air case. Figs. 32 and 33 give the results for a non-catalytic wall. A reduction in heating rate of

40 percent over the fully catalytic case has been assumed based on the results for HRSI materials [15].

The computational grid for EBROEC is shown in fig. 34. Results for the EBROEC are presented in figs. 35 to 39. The calculations are carried out for $M_\infty = 20$ and $H = 280,000$ ft. Figs. 40 and 41 show a comparison of heat transfer calculated by the present method with some experimental [17] and computational results [20] for spherical cone. The results agree well with the experimental and the detailed analysis for most of the body. However, the present method underpredicts the heating rates for the corner. This seems to be acceptable for a preliminary design. Figs. 42 and 43 show a comparison of heat transfer calculated by the present method with some experimental and computational results [13] for EBROEC. These seem to agree well except at the stagnation region. The values predicted by the present method are on the higher side in that region. Fig. 44 shows the pressure distribution obtained by modified Newtonian theory. Comparing it with the numerical solution for axisymmetric Eulers equations, it can be seen that the pressure gradient is overpredicted in the nose and corner regions, and is zero for the cone region. Due to this, in fig. 45, the heating rates calculated are higher in the stagnation region and lower in the flat conical region. Similar results for other aeroassist vehicle shape are shown in [18, 23]. It is also concluded in [23] that modified Newtonian theory is not reliable for the Aeroassisted Flight Experiment Vehicle.

Chapter 5. Conclusions

5.1 Overview

A method has been developed for the calculation of heat transfer and wall temperatures for Aeroassisted Orbital Transfer Vehicles. Results have been obtained for two configurations under various reentry conditions.

The results show that the heating rates are highest at the stagnation region and taper off quite rapidly. This can be used for reducing the thickness of the surface insulation material away from the stagnation region. The turbulent heating rate calculations show that the maximum value of the heating rate can occur away from the stagnation region. However, these calculations were carried out assuming a turbulent flow in a flow regime which is normally laminar in nature. Thus the correctness of the result is doubtful.

The results are in good agreement with detailed calculations and experimental results [13,17,20]. Thus the present method can be effectively used for design calculations at a fraction of the computational effort. The maximum error in heat transfer was about 15 percent which results in an error of less than 5 percent in the wall temperatures. After

carrying out a trajectory analysis, the non-dimensionalized heat transfer can be used to calculate heating rates at various points along the trajectory. The maximum heating rate along the trajectory can be found from these calculations.

5.2 Suggestions for Future Work

Present calculations neglect the radiative heat transfer to the heat-shield and assume no variation in insulation material. However, in some cases, the non-equilibrium radiative heating rates can be quite high and change the total heating rates considerably. A combination of insulating materials with different catalytic values produces spikes in the heat transfer at the junctions of these materials. Simplified methods for the calculation of heating rates taking these phenomena into account provide good research problems

List of References

1. London, H.S., "Change of Satellite Orbit Plane by Aerodynamic Maneuvering", *Journal of Aerospace Sciences*, Vol. 29, March 1962, pp. 323-332.
2. Walberg, G.D., "A survey of Aeroassisted Orbit Transfer", AIAA 82-1378, AIAA 9th Atmospheric Flight Mechanics Conference, Aug. 1982.
3. "Design Study of an Integrated Aerobraking Orbital Transfer Vehicle", NASA Technical Memorandum 58264, March 1983.
4. Scott, C.D., Reid, R.C., Maraia, R.J., Li, C.P. and Derry, S.M., "An AOTV Aeroheating and Thermal Protection Study", AIAA 84-1710, AIAA 19th Thermophysics Conference, June 1984.
5. Thomas, J.L. and Walters, R.W., "Upwind Relaxation Algorithms for the Navier Stokes Equations", AIAA 85-1501, AIAA 7th Computational Fluid Dynamics Conference, July 1985.
6. Van Leer, B., "Flux-Vector Splitting for the Euler Equations", ICASE Report No. 82-30, Sept. 1982.
7. Walters, R.W. and Dwoyer, D.L., "An Efficient Strategy Based on Upwind/Relaxation Schemes for the Euler Equations", AIAA 85-1529, AIAA 7th Computational Fluid Dynamics Conference, July 1985.
8. Thomas, J.L., Van Leer, B. and Walters, R.W., "Implicit Flux Split Schemes for the Euler Equations", AIAA 85-1680, AIAA 18th Fluid Dynamics and Plasmadynamics and Lasers Conference, July 1985.

9. Grossman, B. and Walters, R.W., "An Analysis of Flux-Split Algorithms for Euler's Equations with Real Gases", AIAA 87-1117, AIAA 8th Computational Fluid Dynamics Conference, June, 1987.
10. Cohen, N.B., "Boundary-Layer Similar Solutions and Correlation Equations for Laminar Heat-Transfer Distribution in Equilibrium Air at Velocities up to 41,100 Feet Per Second", NASA TR R-118, 1961.
11. Sutton, K. and Graves, R.A., Jr., "A General Stagnation Point Convective Heating Equation for Arbitrary Gas Mixtures", NASA TR R-376, Nov. 1971.
12. Zoby, E.V., Moss, J.N. and Sutton, K. "Approximate Convective-Heating Equations for Hypersonic Flows", AIAA 79-1078, AIAA 14th Thermophysics Conference, June 1979.
13. Hamilton, H.H., II, and Weilmuenster, K.J., "Calculation of Convective Heating on Proposed Aeroassist Flight Experiment Vehicle", AIAA 86-1308, AIAA/ASME 4th Joint Thermophysics and Heat Transfer Conference, June 1986.
14. Schlichting, H., "Boundary Layer Theory", 4th Ed., McGraw-Hill, New York, 1960.
15. Scott, C.D., "Space Shuttle Laminar Heating with Finite Rate Catalytic Recombination", AIAA 81-1144, AIAA 16th Thermophysics Conference, June 1981.
16. Cheatwood, F.M., DeJarnette, F.R. and Hamilton, H.H., II, "Geometrical Description for a Proposed Aeroassist Flight Experiment Vehicle", NASA Technical Memorandum 87714, July 1986.
17. Weilmuenster, K.J., and Hamilton, H.H., II, "A Comparison of Computed and Experimental Surface Pressure and Heating on 70 ° Sphere Cones at Angles of Attack to 20 ° ", AIAA 86-0567, AIAA 24th Aerospace Sciences Meeting, Jan. 1986.
18. DeJarnette, F.R., Hamilton, H.H., II, Weilmuenster, K.J. and Cheatwood, F.M., "A Review of Some Approximate Methods Used in Aerodynamic Heating Analyses", AIAA 85-0906, AIAA 20th Thermophysics Conference, June 1985.
19. Tong, H., "User's Manual, Nonequilibrium Chemistry Boundary Layer Integral Matrix Procedure", Part I, Aerotherm. Report UM-73-37, July 1973.
20. Hamilton, H.H., II and Spall, John R., "A Finite-Difference Solution to the Nonsimilar, Axisymmetric Boundary Layer Equations in CF₄ and Equilibrium Air", Proposed NASA TM.
21. Maraia, Robert J., "Data on the Thermal Properties of AFE Aerobrake TPS Materials", NASA note ES32-87-35M, April 14, 1987.

22. Menees, Gene P., Park, Chul and Wilson, John F., "Design and Performance Analysis of a Conical Aerobrake Orbital Transfer Vehicle Concept", AIAA 84-0410, AIAA 22nd Aerospace Sciences Meeting, Jan. 1984.
23. Micol, J.R., "Simulation of Real-Gas Effects on Pressure Distributions for a Proposed Aceroassist Flight Experiment Vehicle and Comparison to Prediction", AIAA 87-2368, AIAA Atmospheric Flight Mechanics Conference, Aug. 1987.

TABLE 1. Geometrical description of spherical cone

Cone half angle	70 degrees
Cone base radius	20 m
Nose sphere radius	10 m
Corner skirt radius	5 m

TABLE 2. Geometrical description of EBROEC

Rake angle	73 degrees
Cone angle (X-Y plane)	60 degrees
Reference circle radius	20 m
Corner skirt angle	60 degrees
Corner skirt radius	4 m
Nose ellipticity ratio (X-Y plane)	2

TABLE 3. Atmospheric conditions

H = 220,000 ft

Pressure P_∞	8.5436 N/m^2
Density ρ_∞	1.2875e-4 kg/m^3
Temperature T_∞	231.23 $^\circ K$

H = 250,000 ft

Pressure P_∞	2.0340 N/m^2
Density ρ_∞	3.6255e-5 kg/m^3
Temperature T_∞	195.46 $^\circ K$

H = 280,000 ft

Pressure P_∞	0.3872 N/m^2
Density ρ_∞	7.4676e-6 kg/m^3
Temperature T_∞	180.65 $^\circ K$

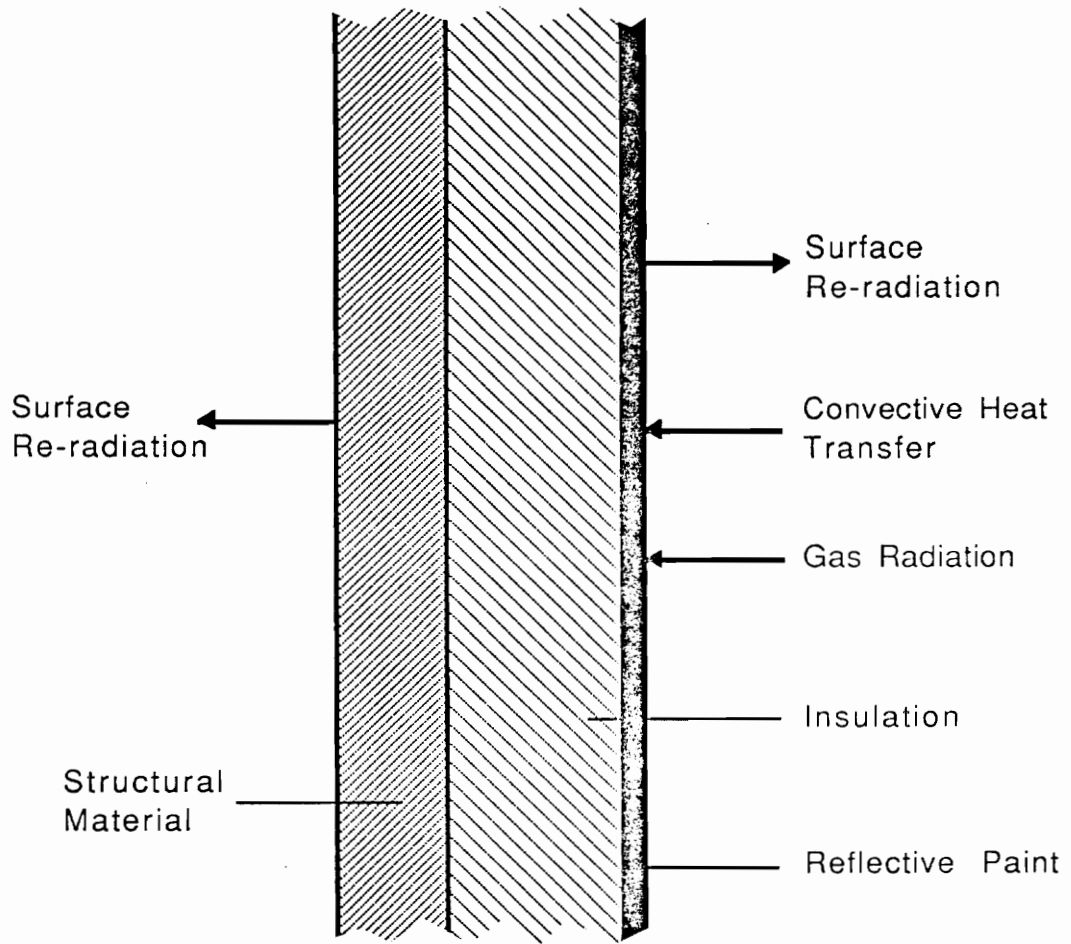


Fig. 1: Thermal Protection System

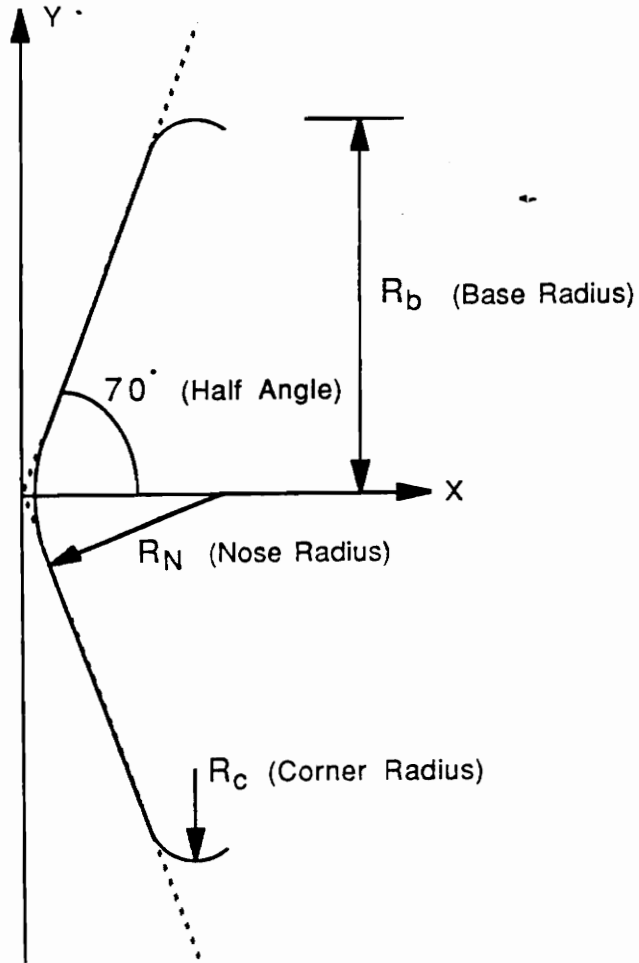


Fig. 2: Spherical Cone Aerobrake Configuration

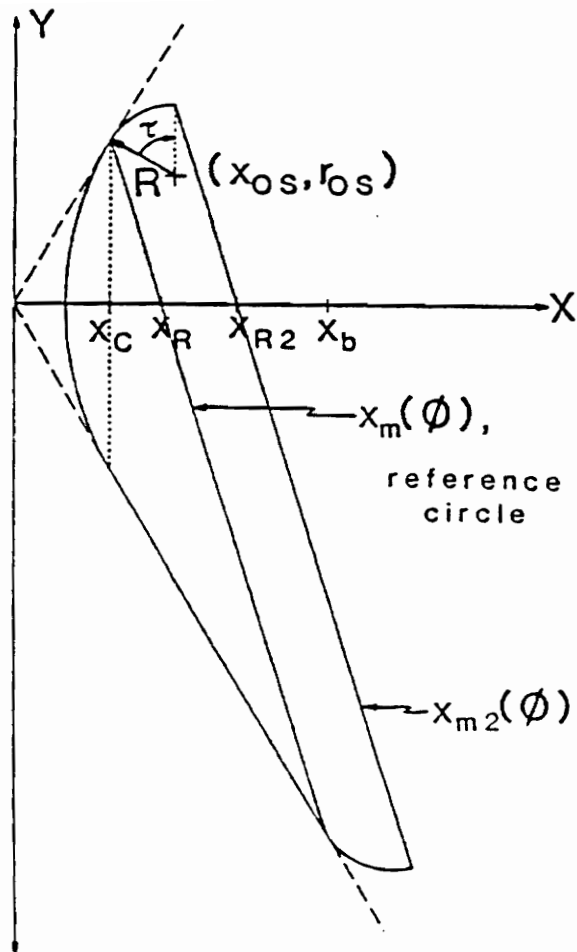


Fig. 3: EBROEC Aerobrake Configuration

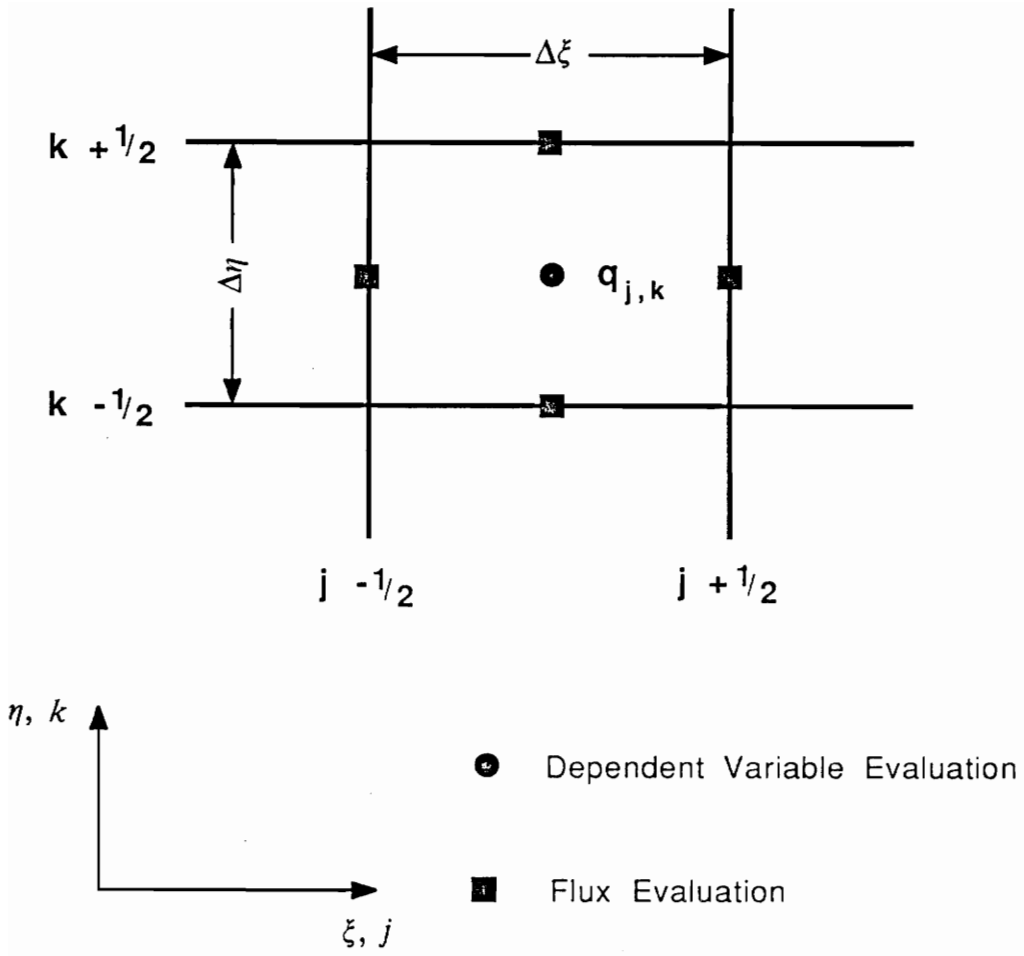


Fig. 4: Notation for cell (j,k)

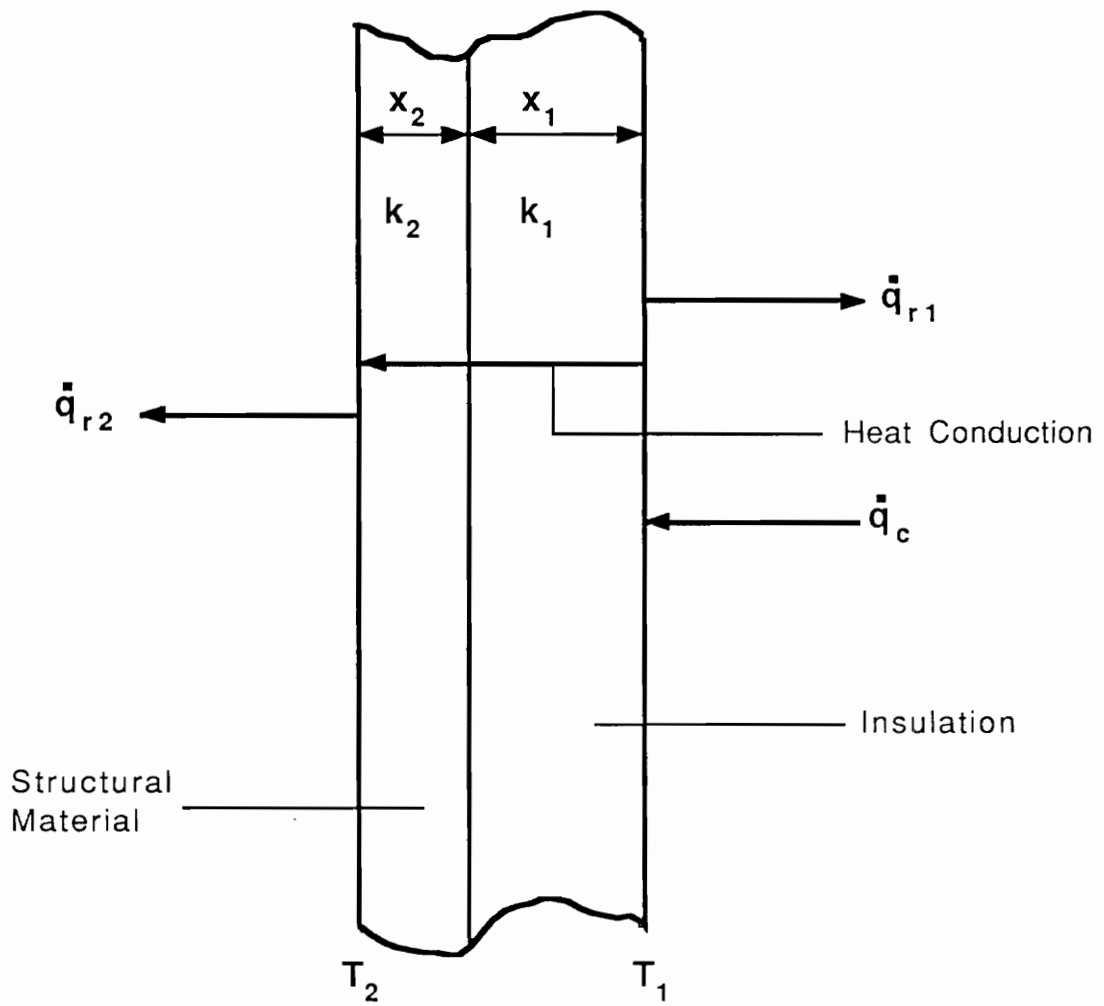


Fig. 5: Heat conduction model with energy balance

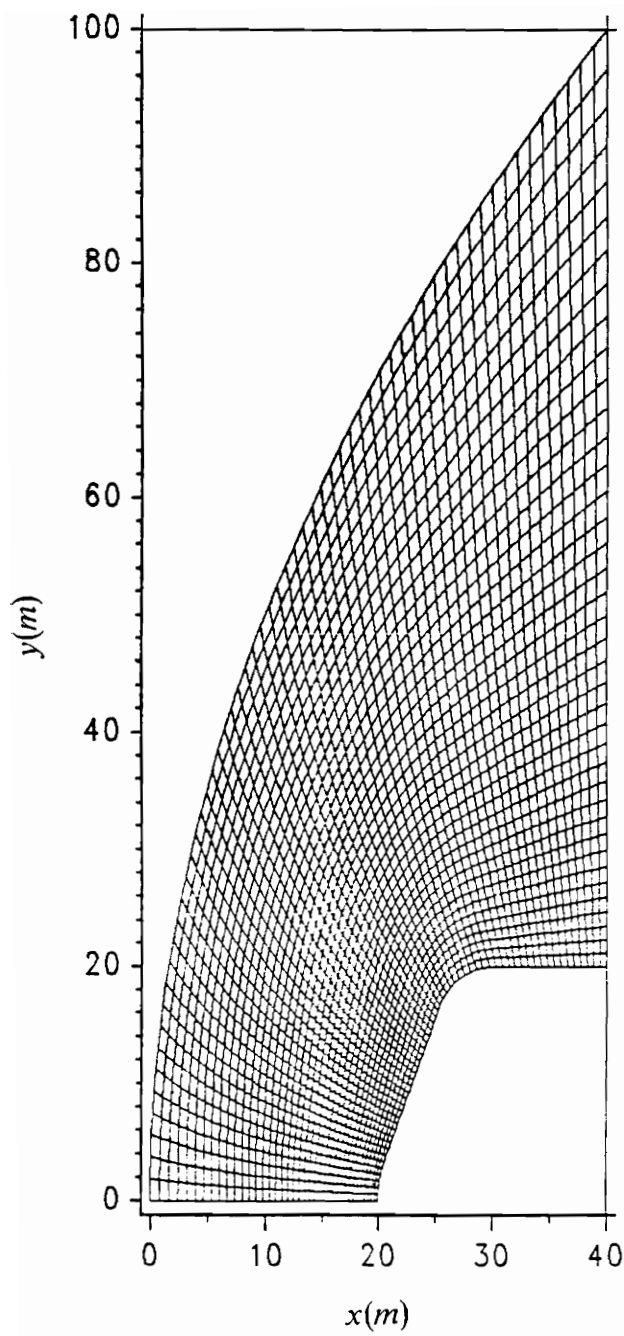


Fig. 6: Computational grid for spherical cone

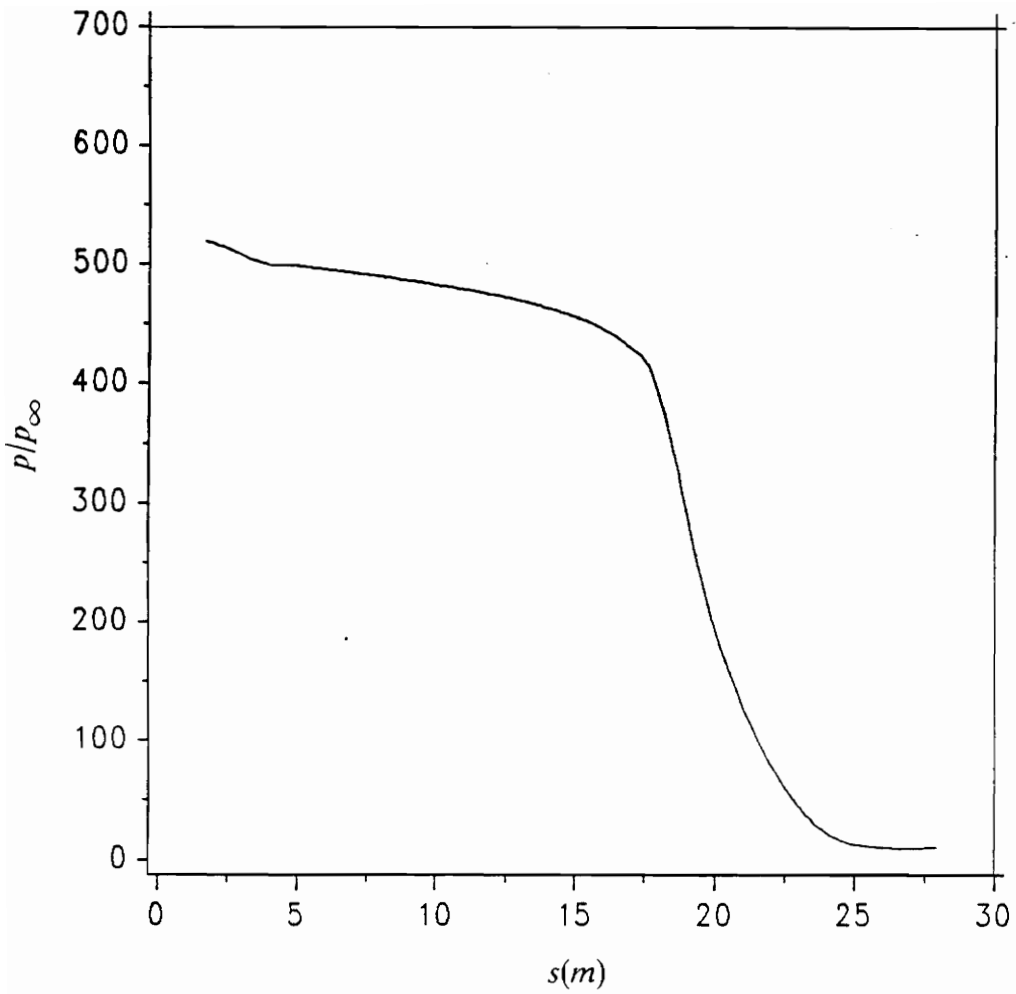


Fig. 7: Boundary layer edge pressure distribution $M_\infty = 20$ (perfect gas)

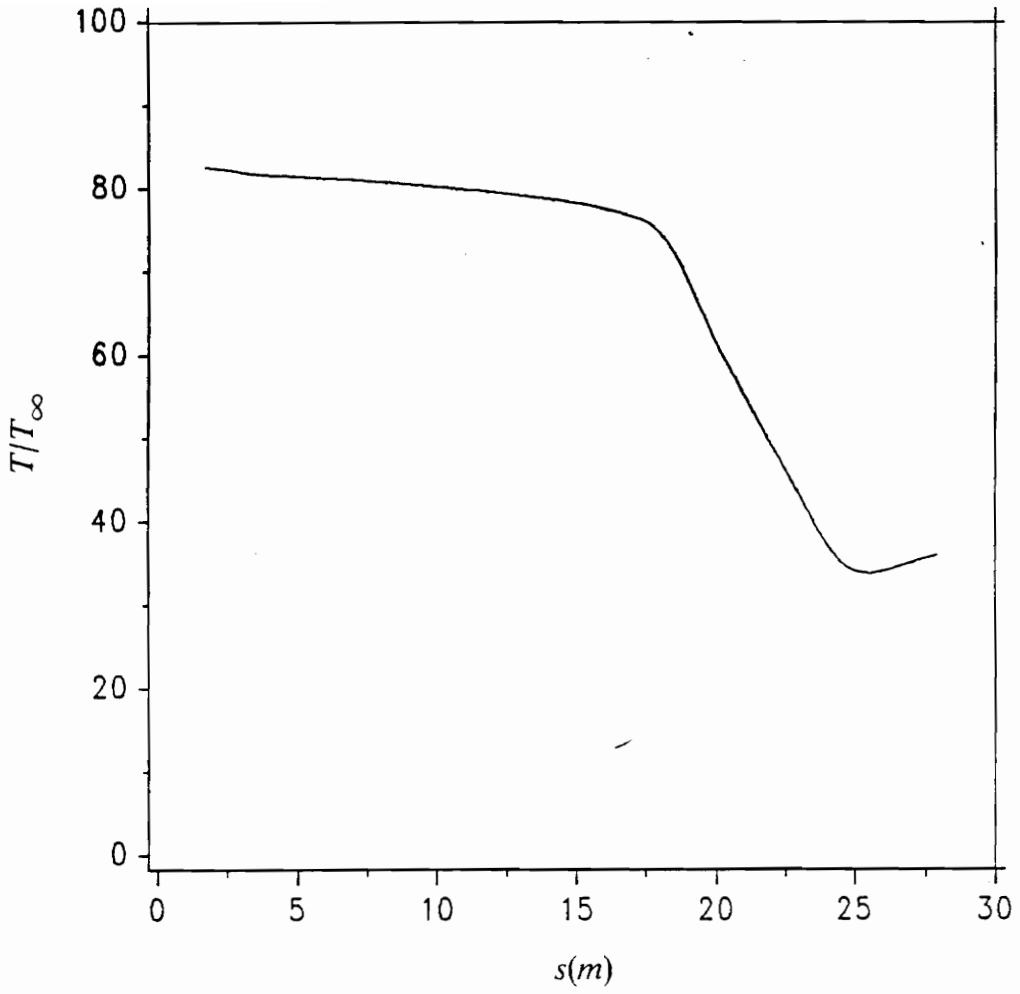


Fig. 8: Boundary layer edge temperature distribution $M_\infty = 20$ (perfect gas)

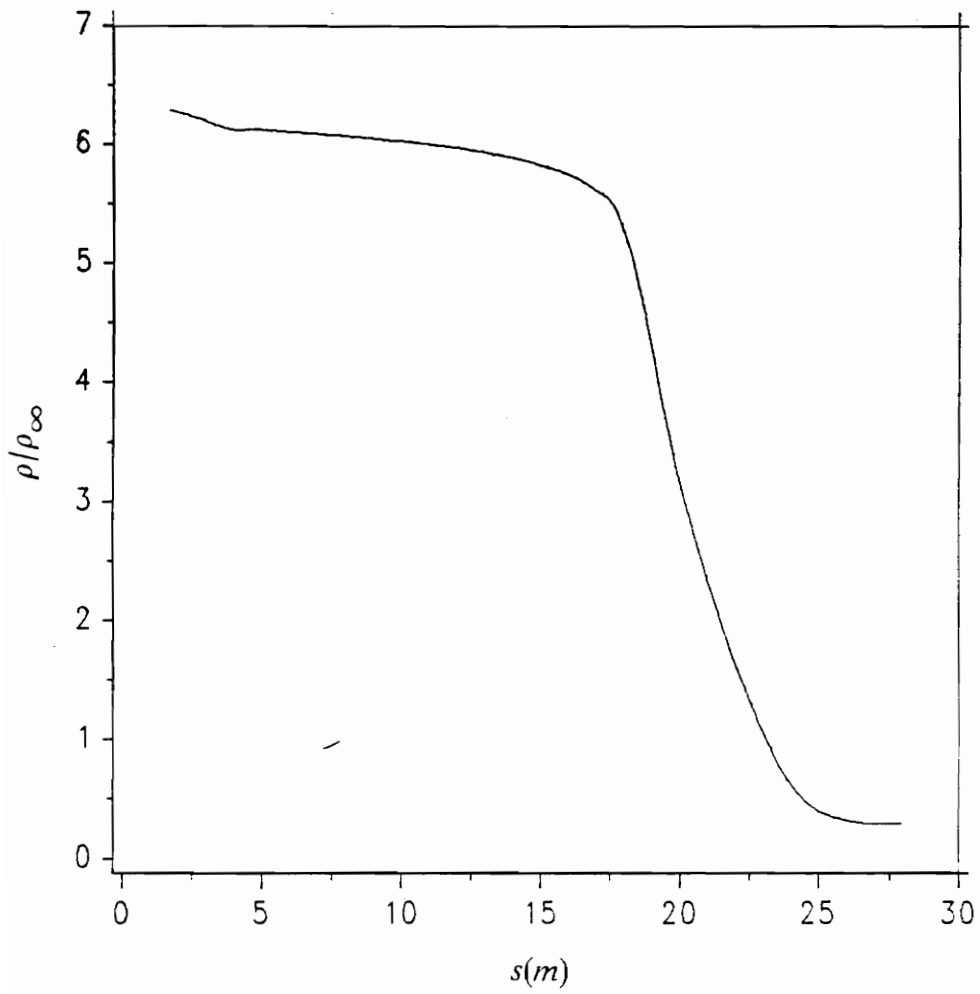


Fig. 9: Boundary layer edge density distribution $M_\infty = 20$ (perfect gas)

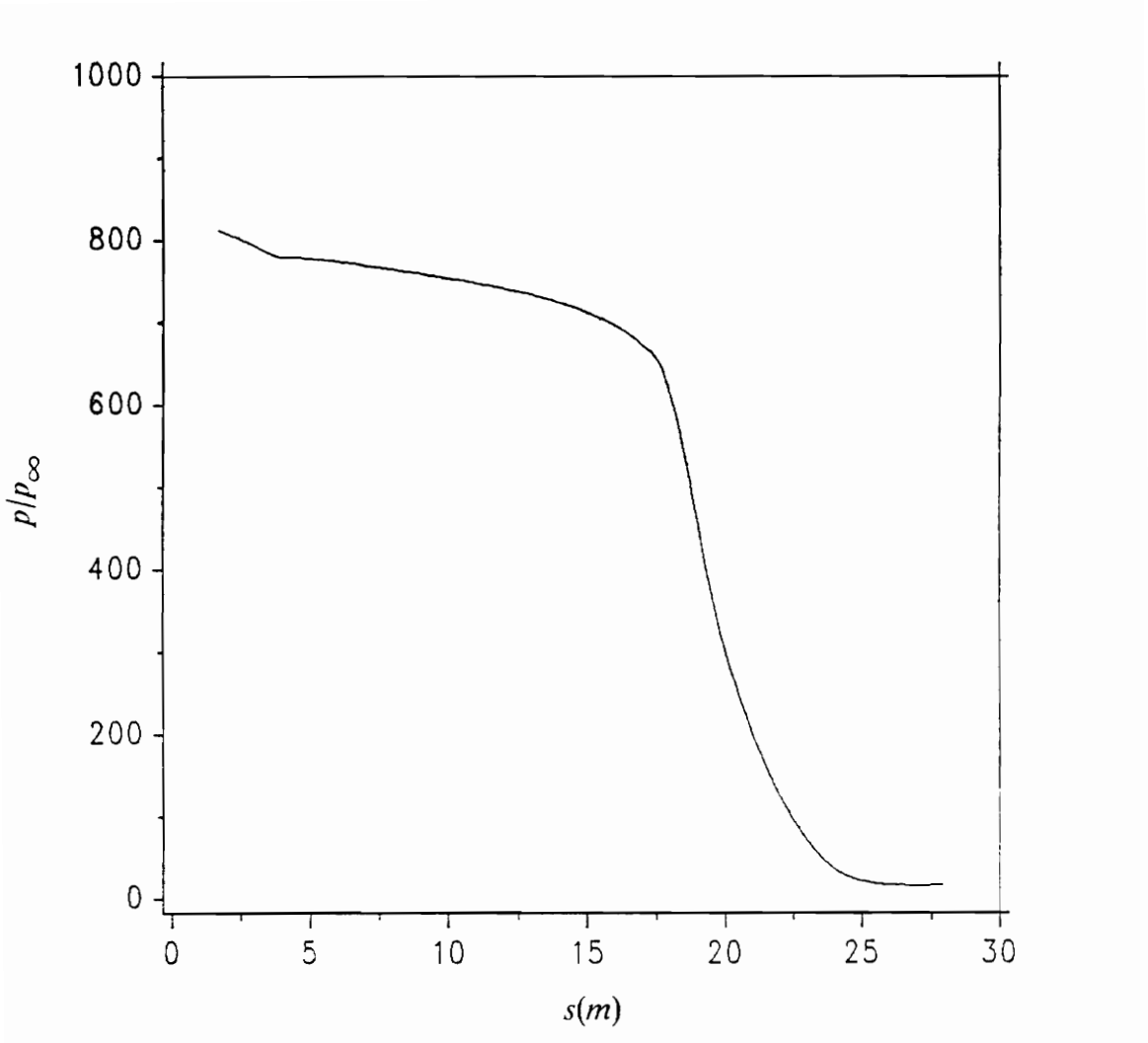


Fig. 10: Boundary layer edge pressure distribution $M_\infty = 25$ (perfect gas)

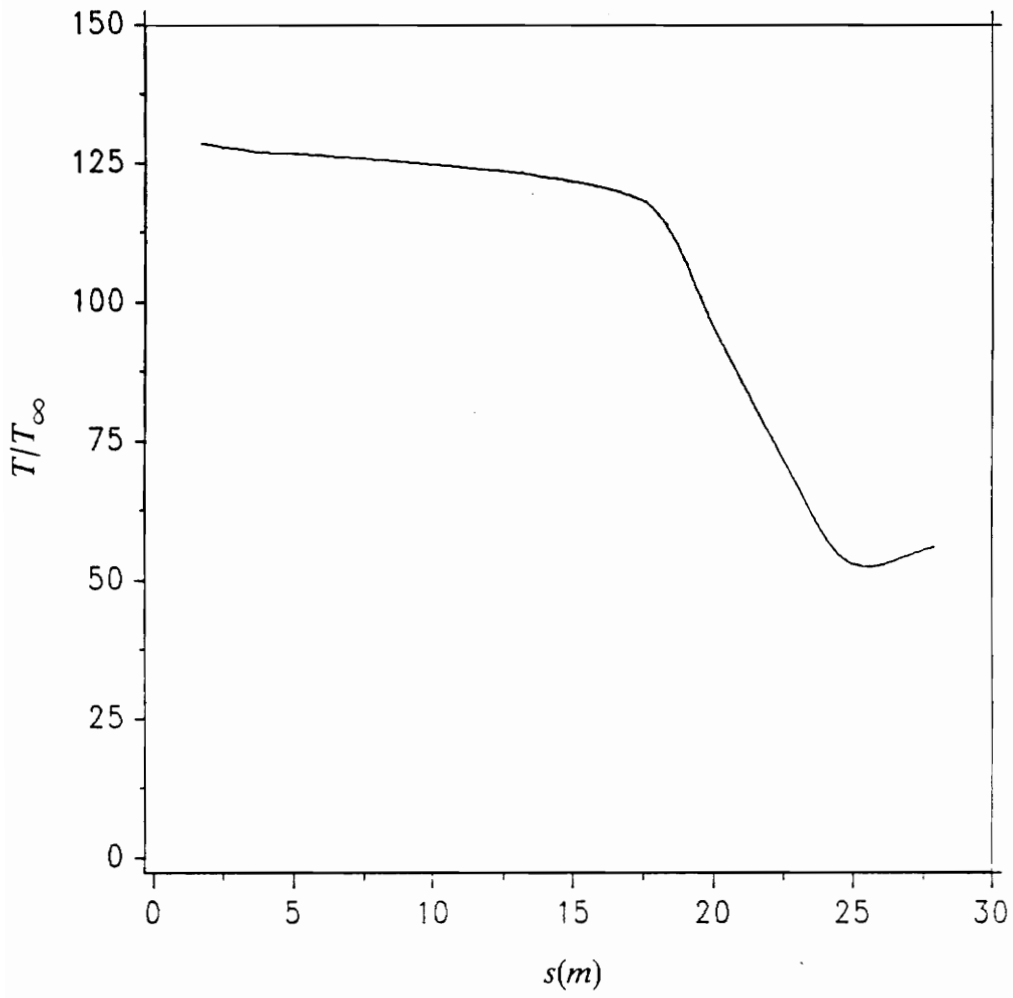


Fig. 11: Boundary layer edge temperature distribution $M_\infty = 25$ (perfect gas)

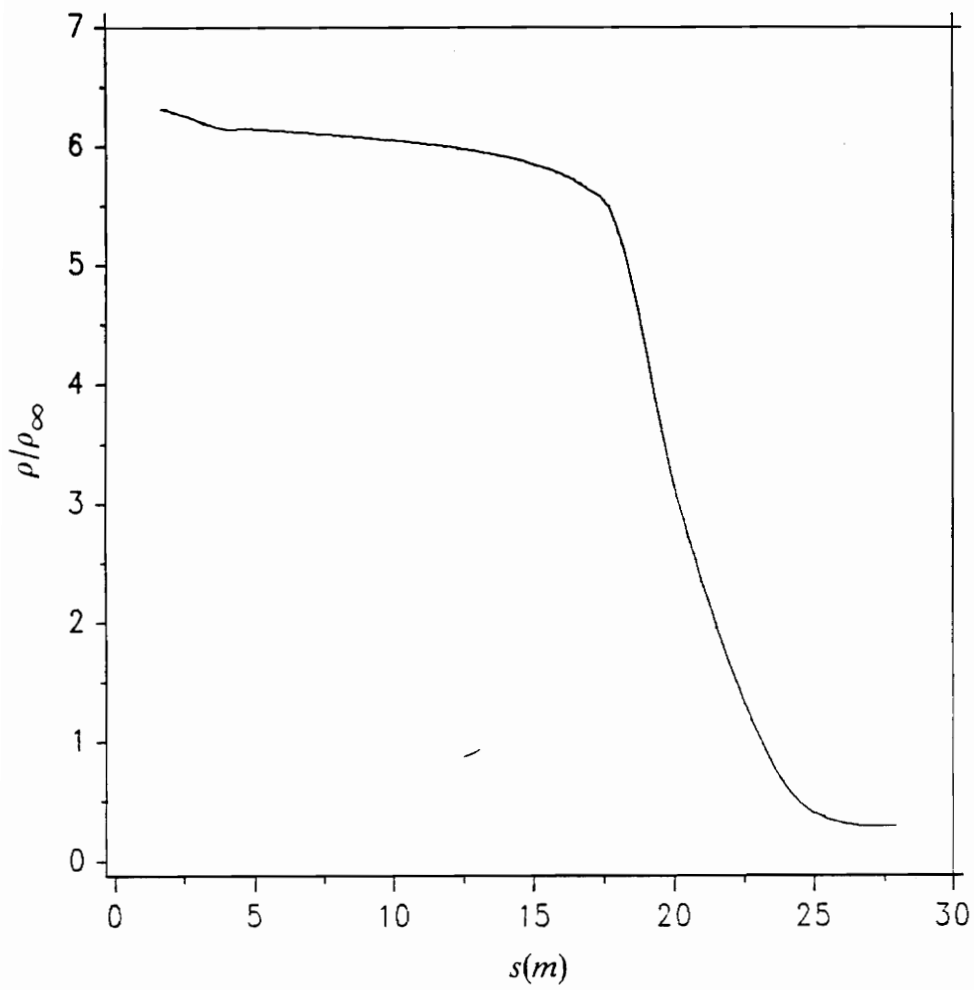


Fig. 12: Boundary layer edge density distribution $M_\infty = 25$ (perfect gas)

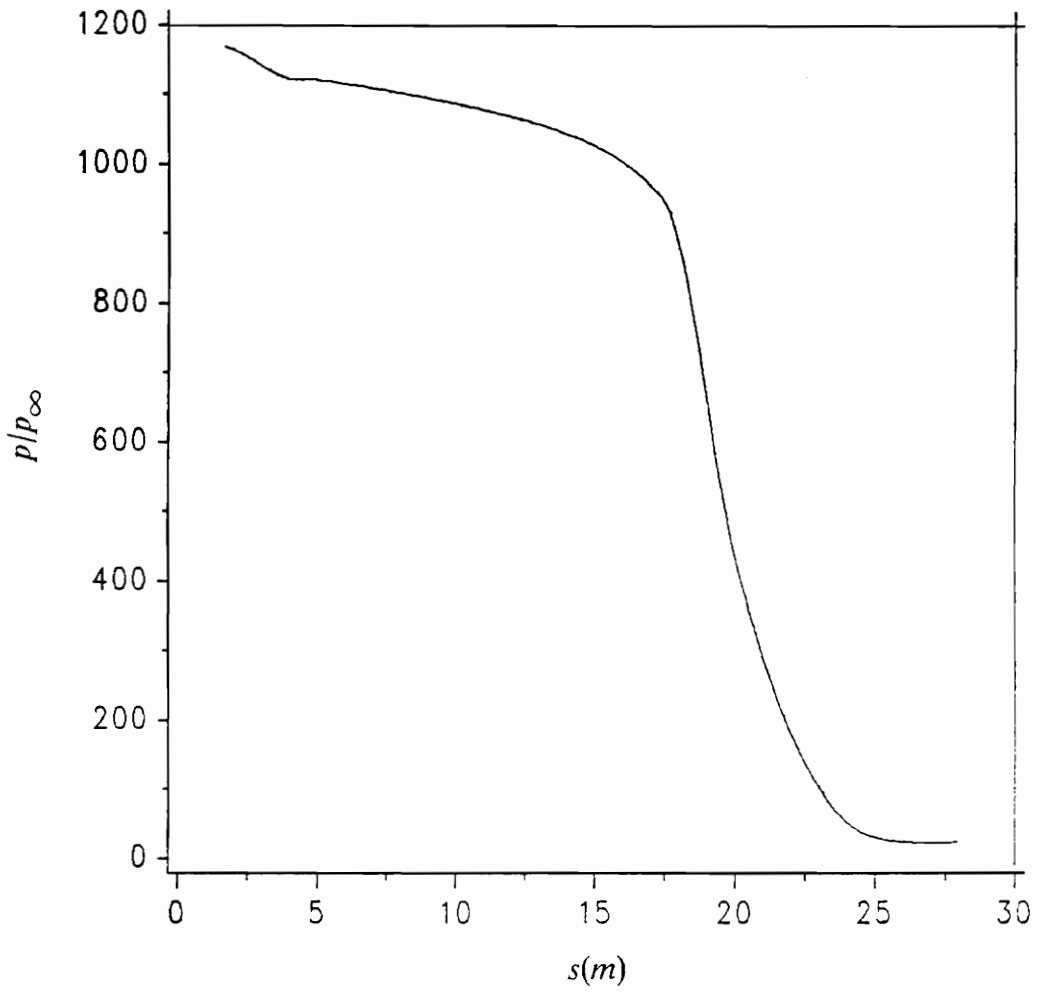


Fig. 13: Boundary layer edge pressure distribution $M_{\infty} = 30$ (perfect gas)

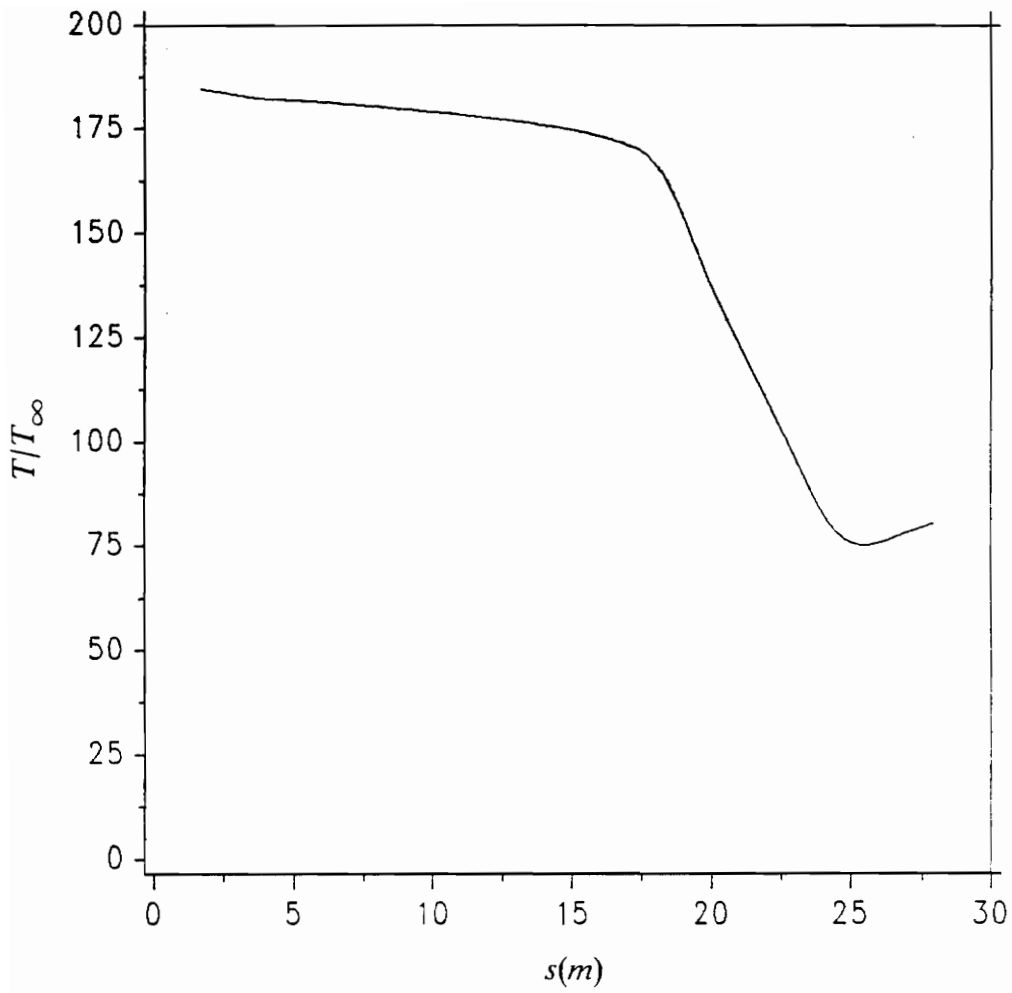


Fig. 14: Boundary layer edge temperature distribution $M_\infty = 30$ (perfect gas)

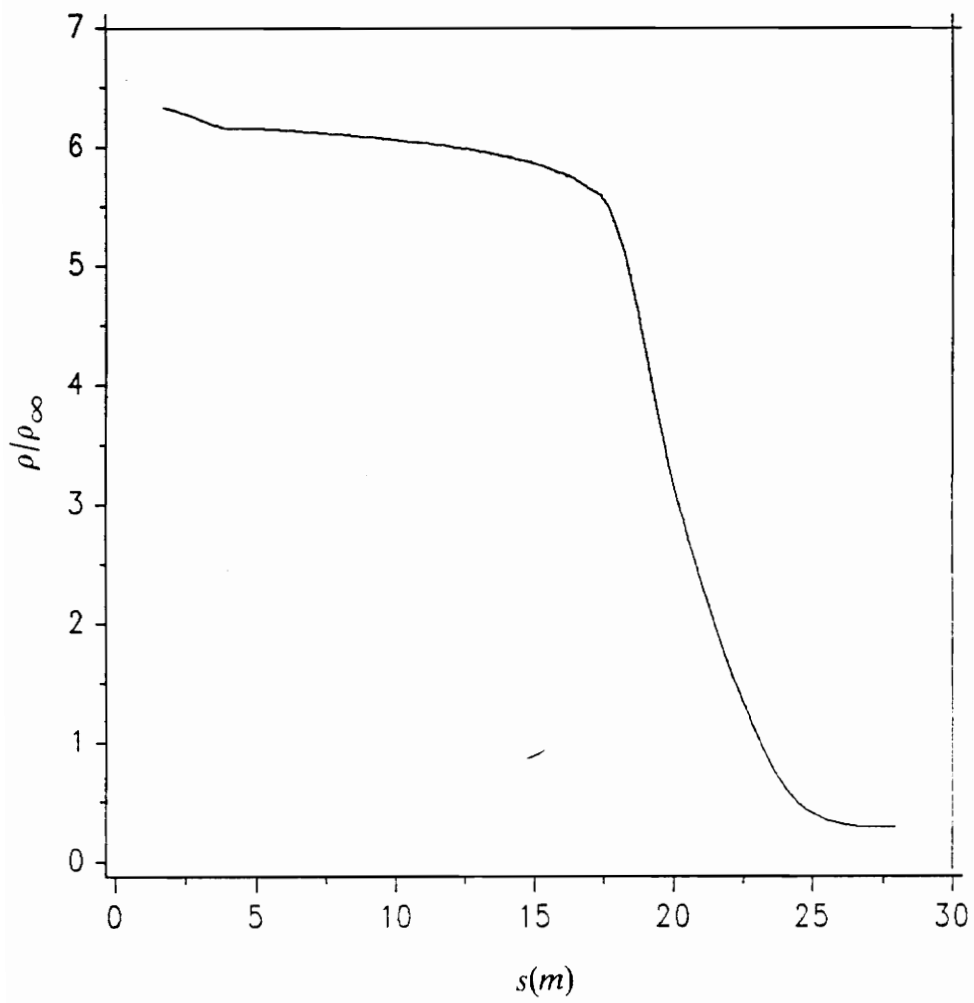


Fig. 15: Boundary layer edge density distribution $M_\infty = 30$ (perfect gas)

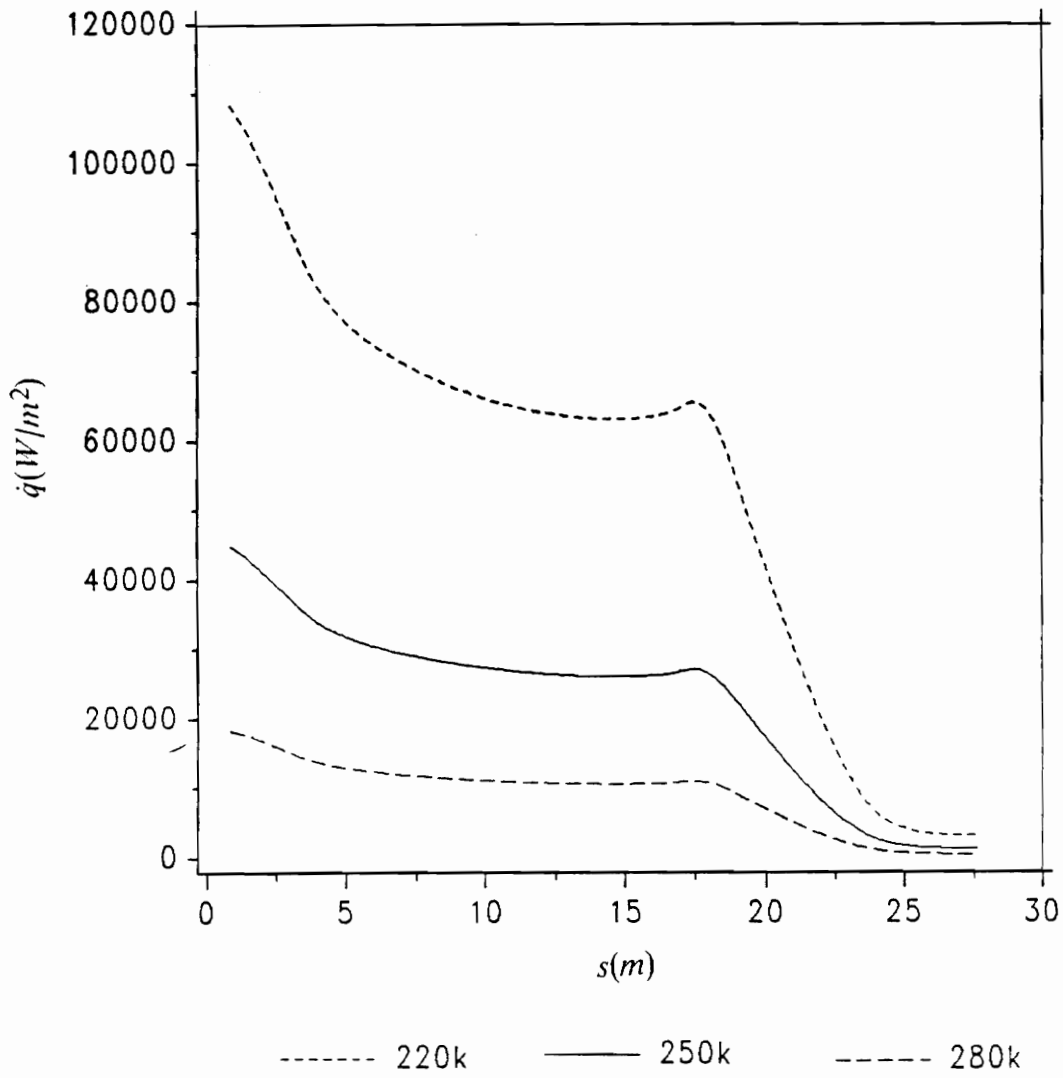


Fig. 16: Variation of heat transfer with altitude

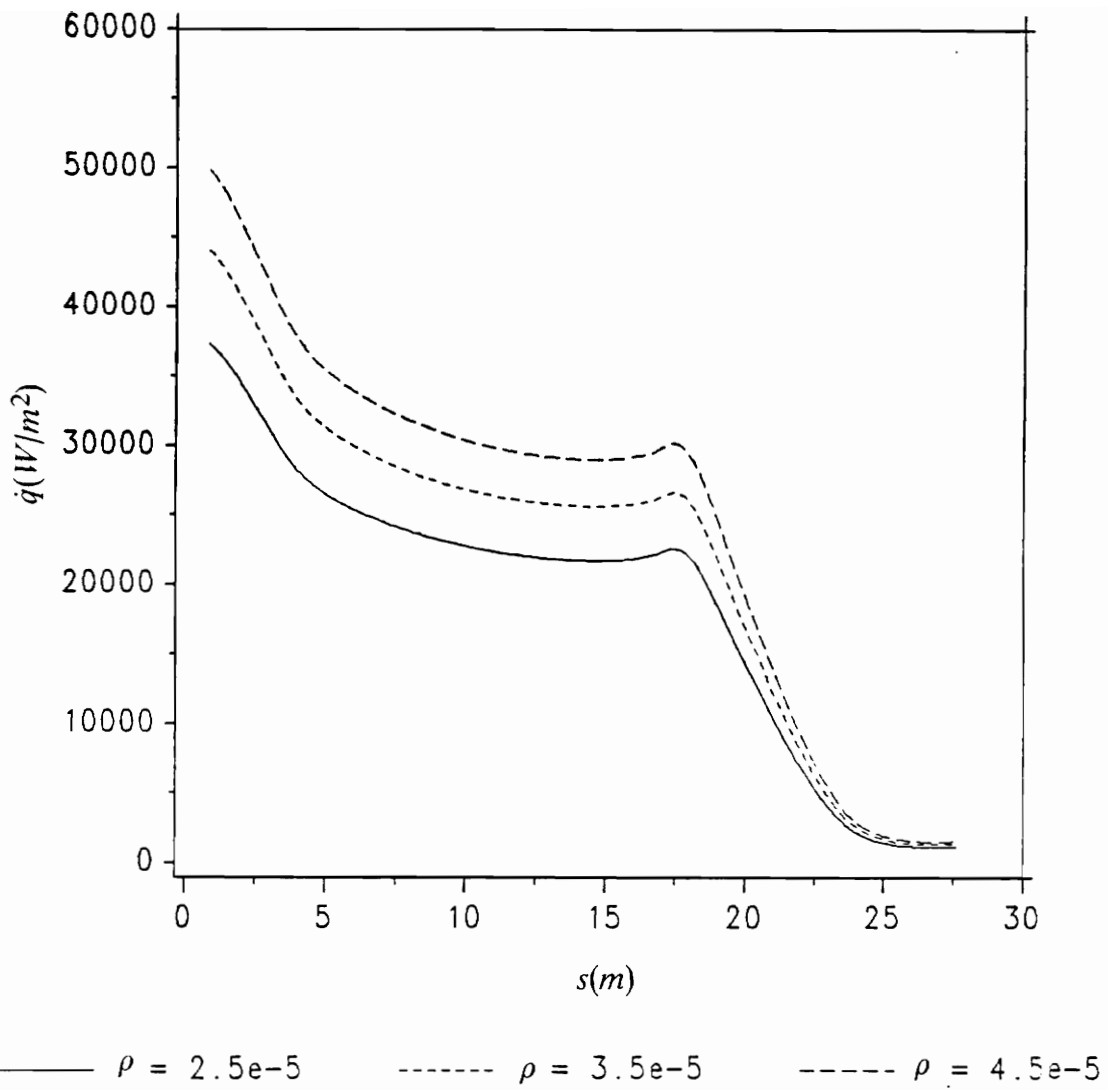


Fig. 17: Variation of heat transfer with ρ_∞

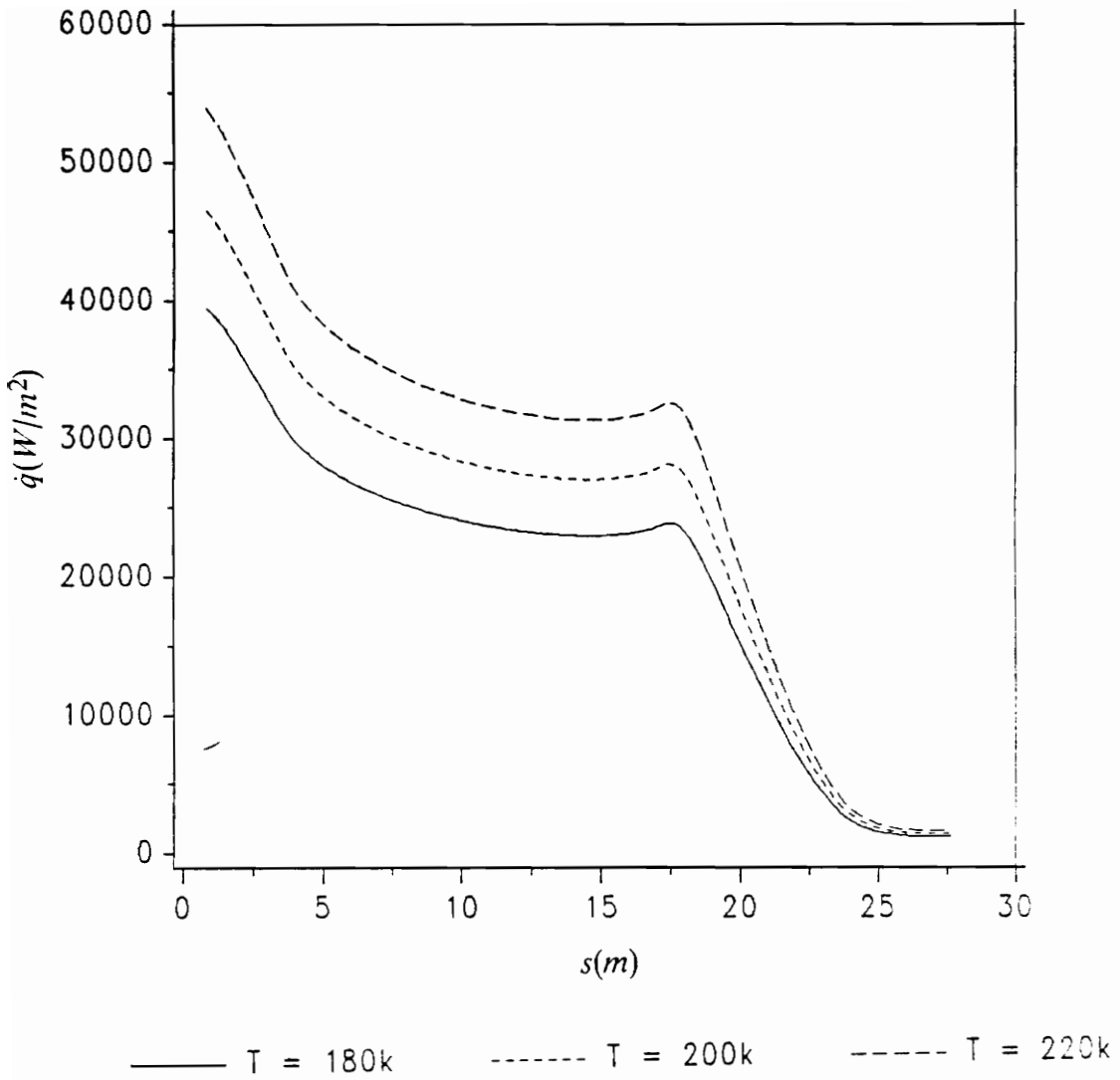


Fig. 18: Variation of heat transfer with T_∞

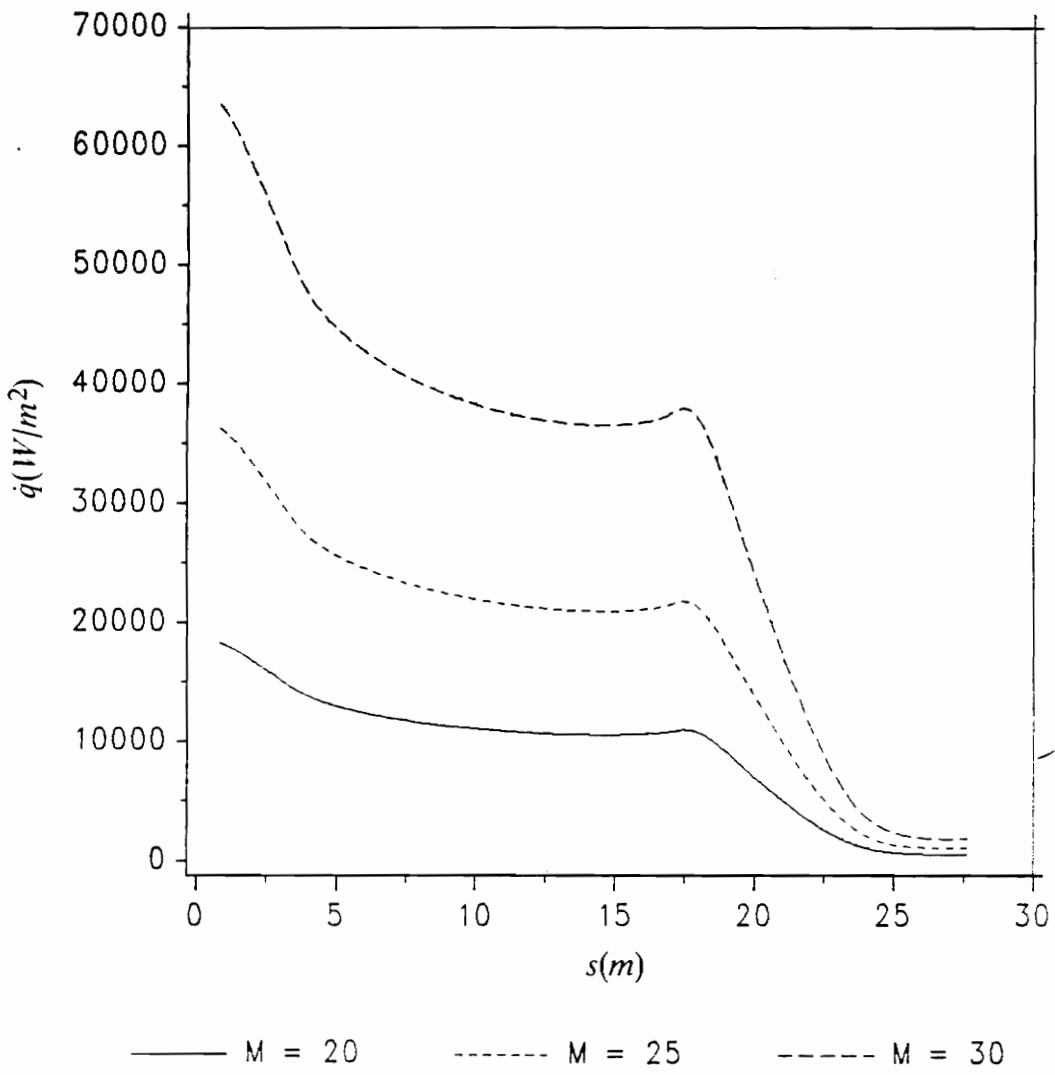


Fig. 19: Variation of heat transfer with Mach number

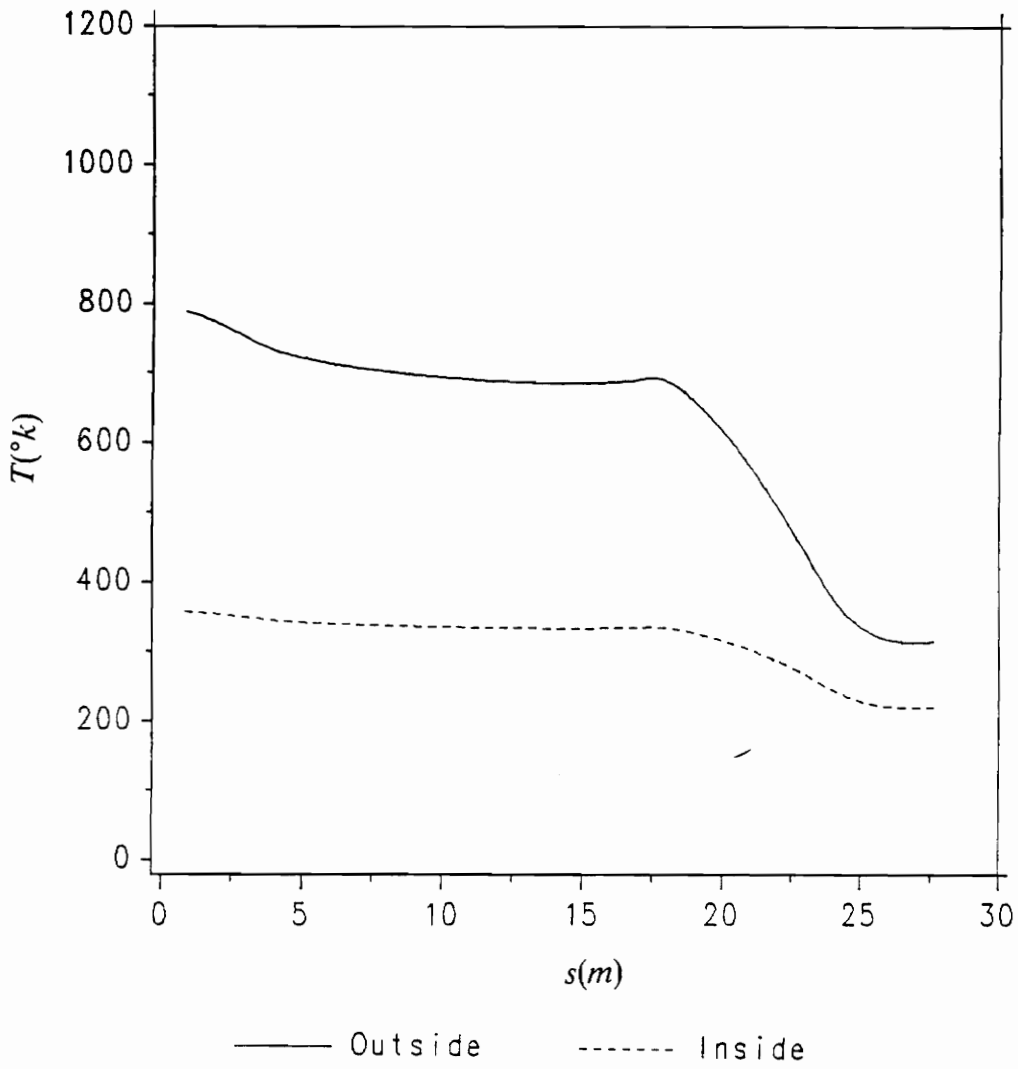


Fig. 20: Wall temperatures $M_\infty = 20$, $H = 280$ kft (perfect gas)

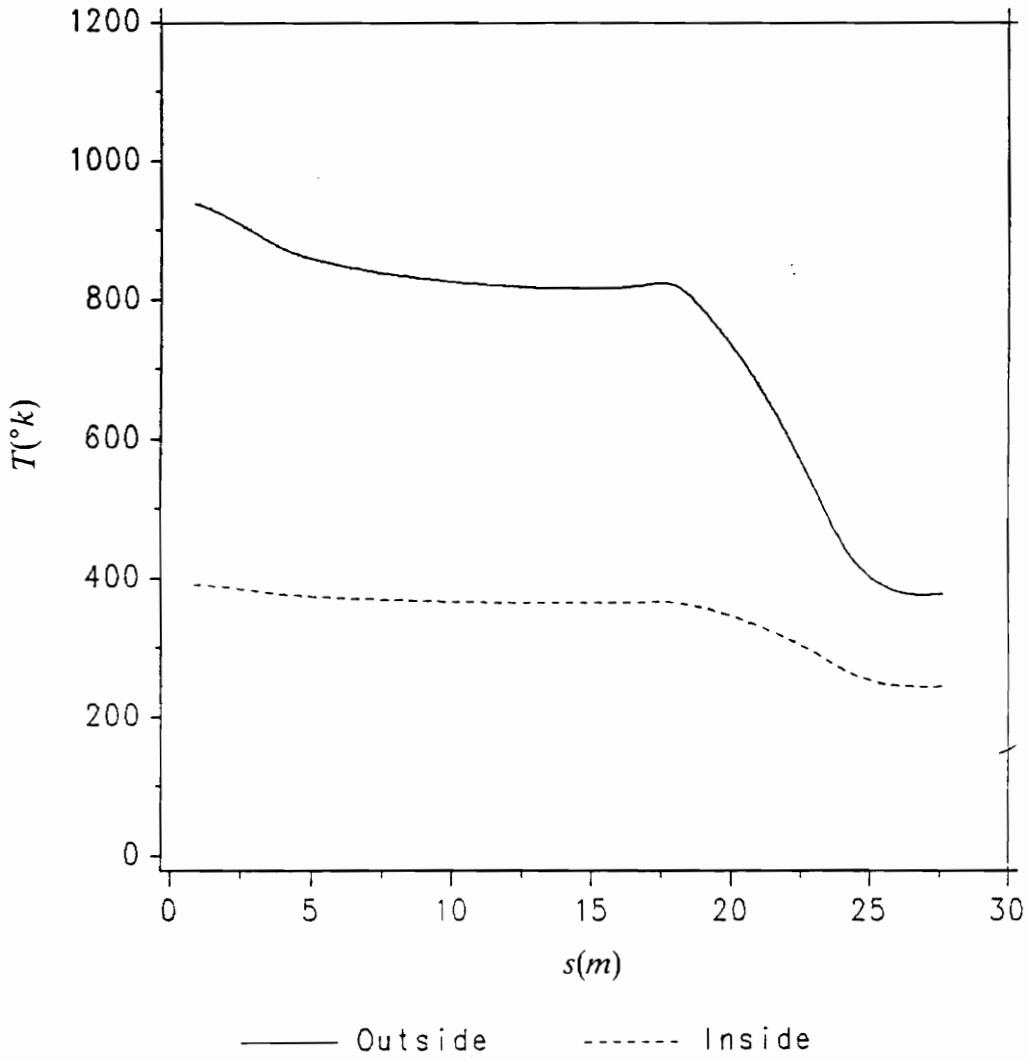


Fig. 21: Wall temperatures $M_\infty = 25$, $H = 280$ kft (perfect gas)

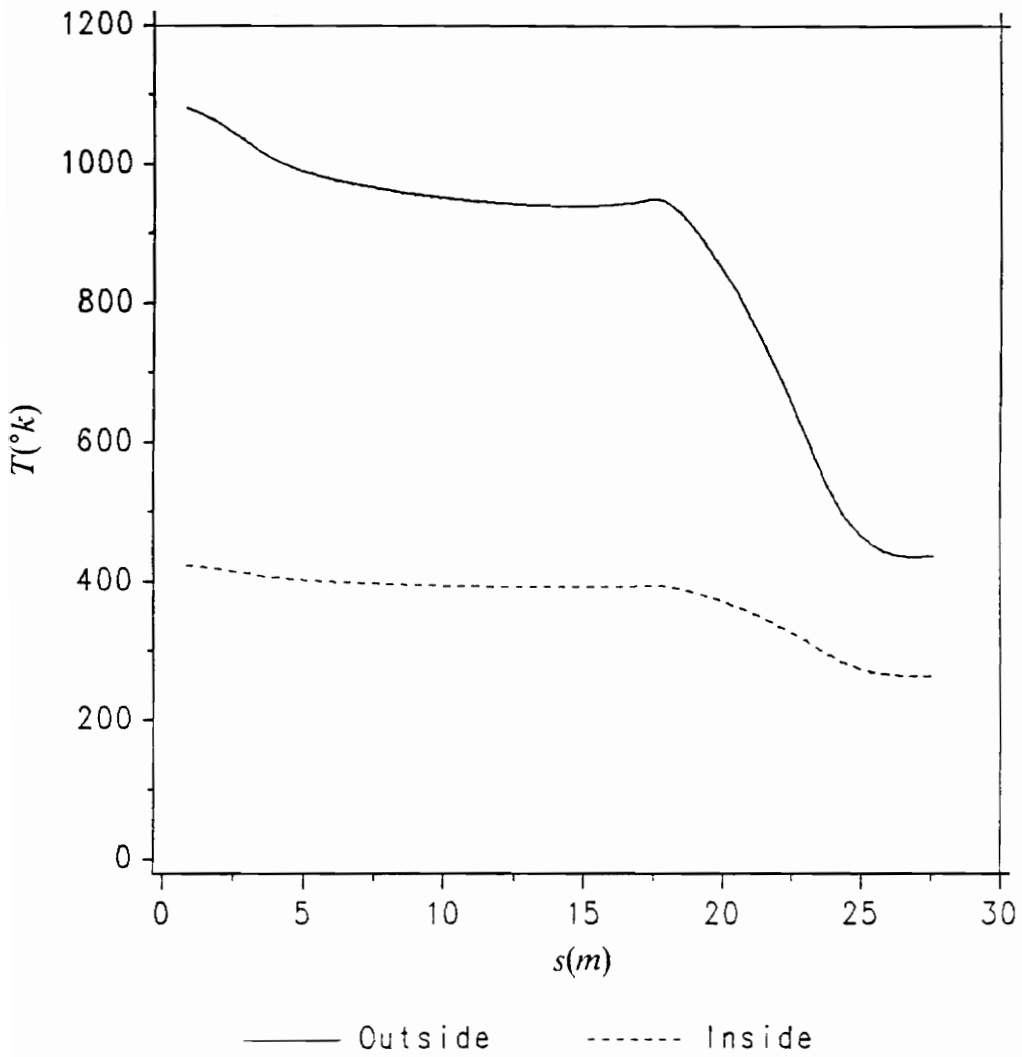


Fig. 22: Wall temperatures $M_\infty = 30$, $H = 280$ kft (perfect gas)

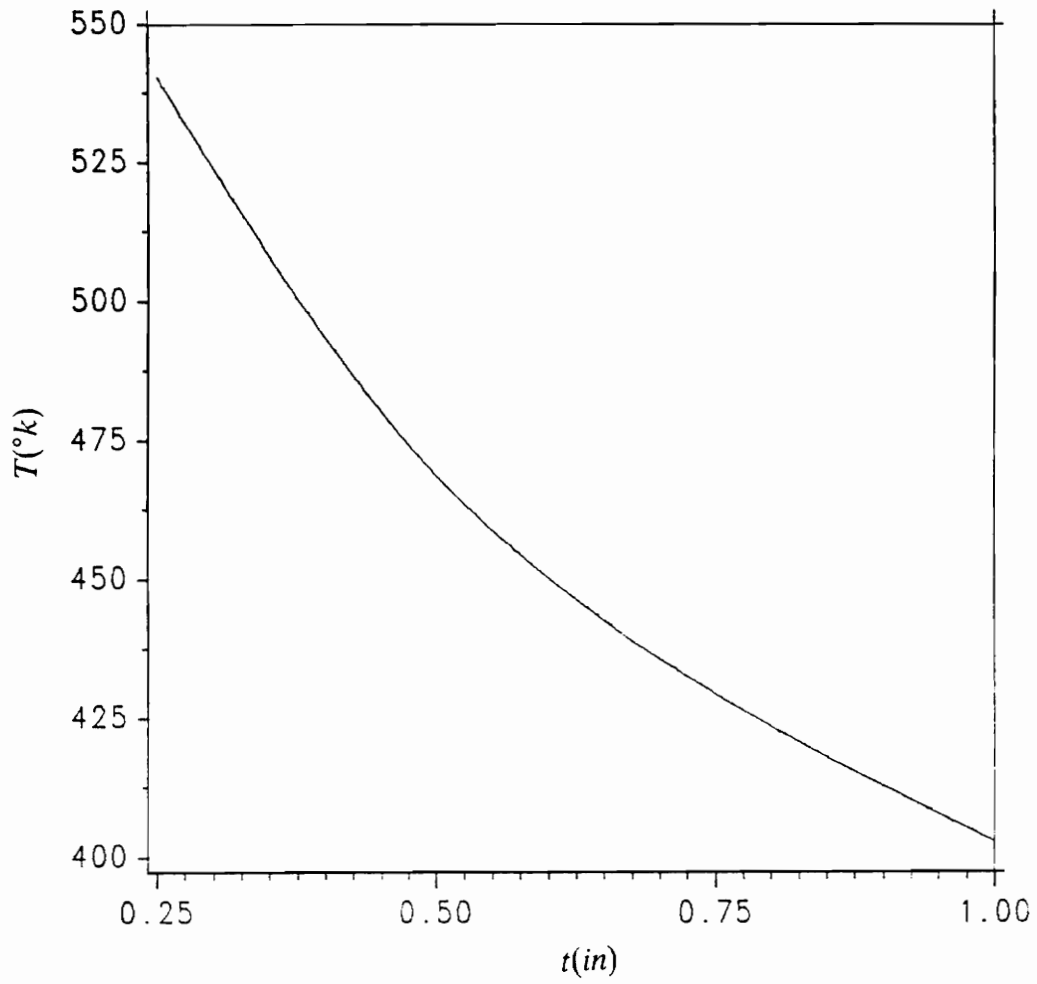


Fig. 23: Variation of inside temperature with insulation thickness

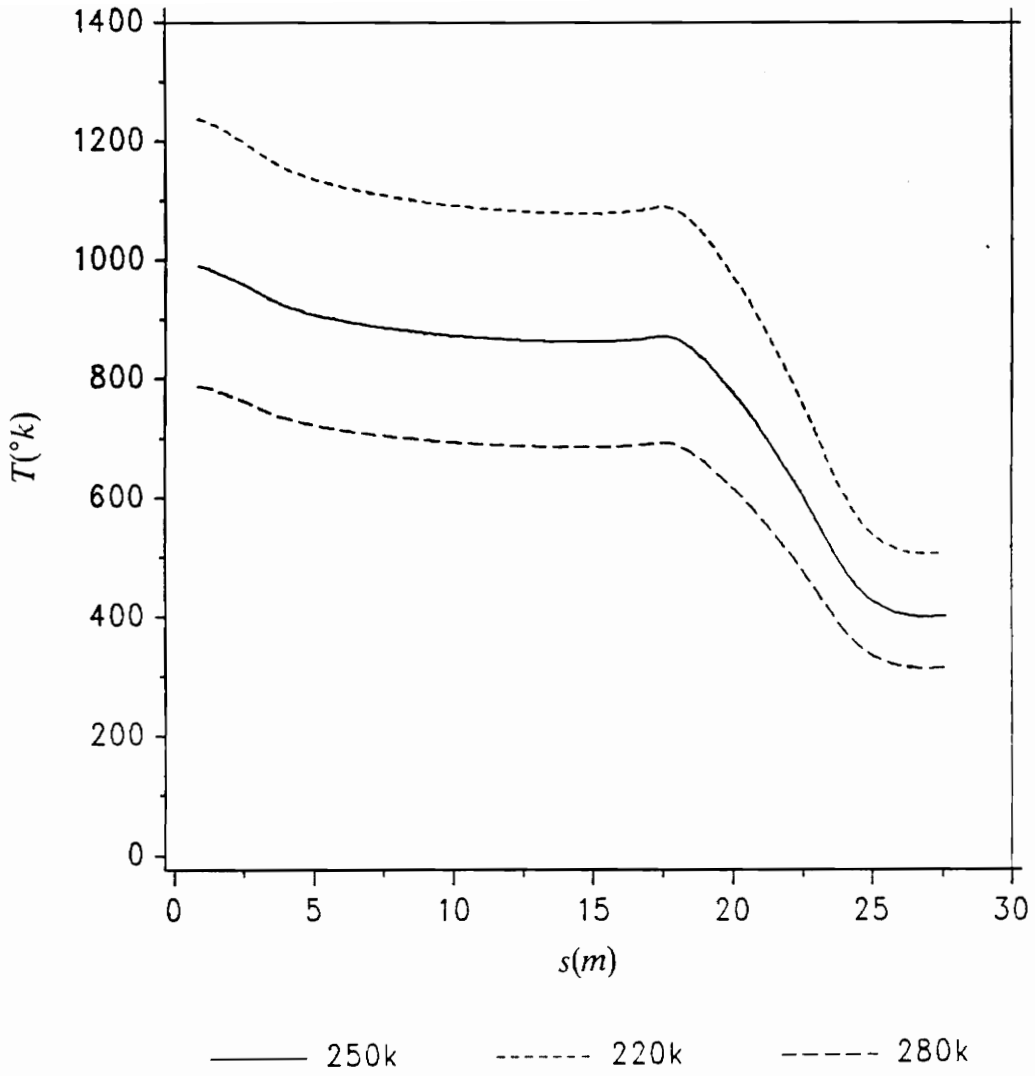


Fig. 24: Variation of surface temperature with altitude

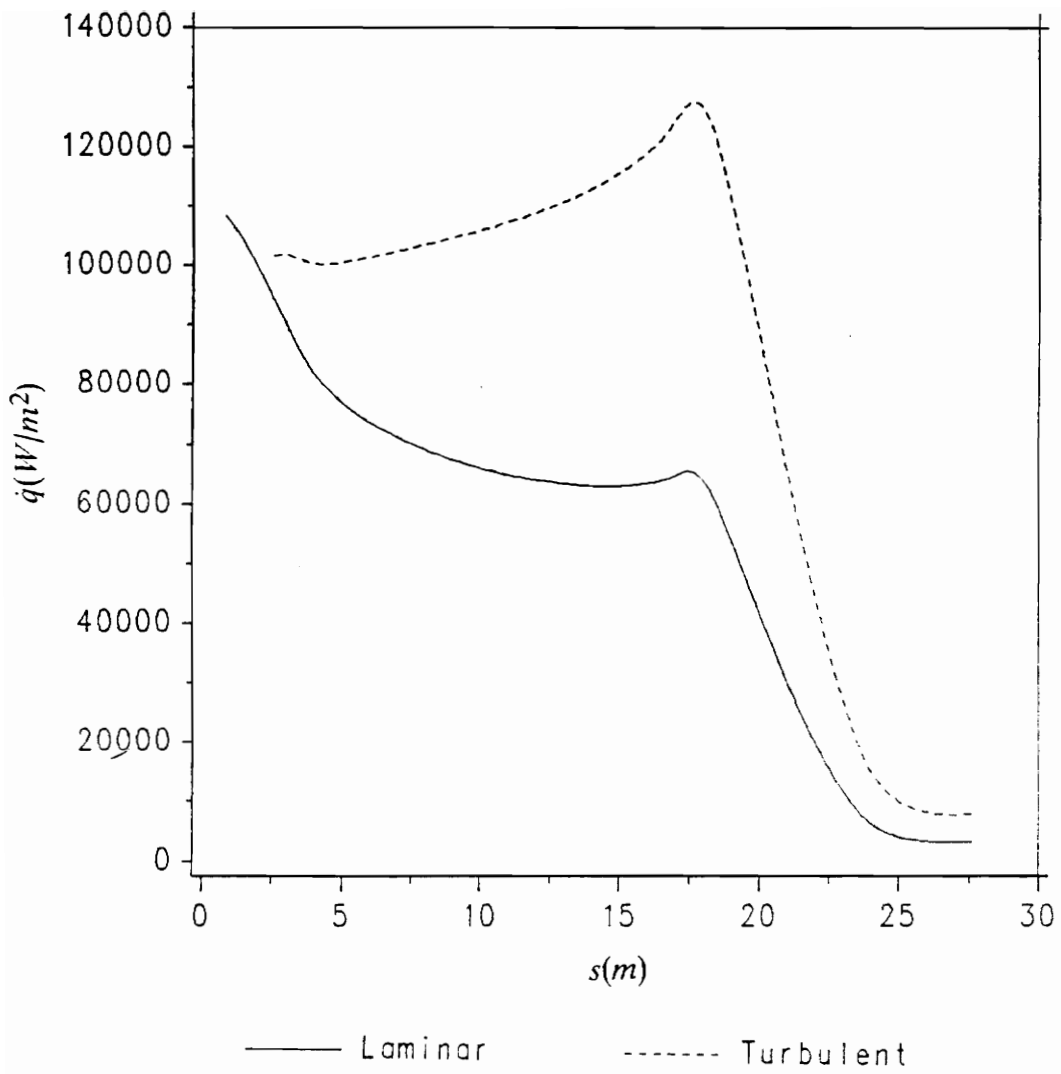


Fig. 25: Comparison of Laminar and Turbulent heating rates

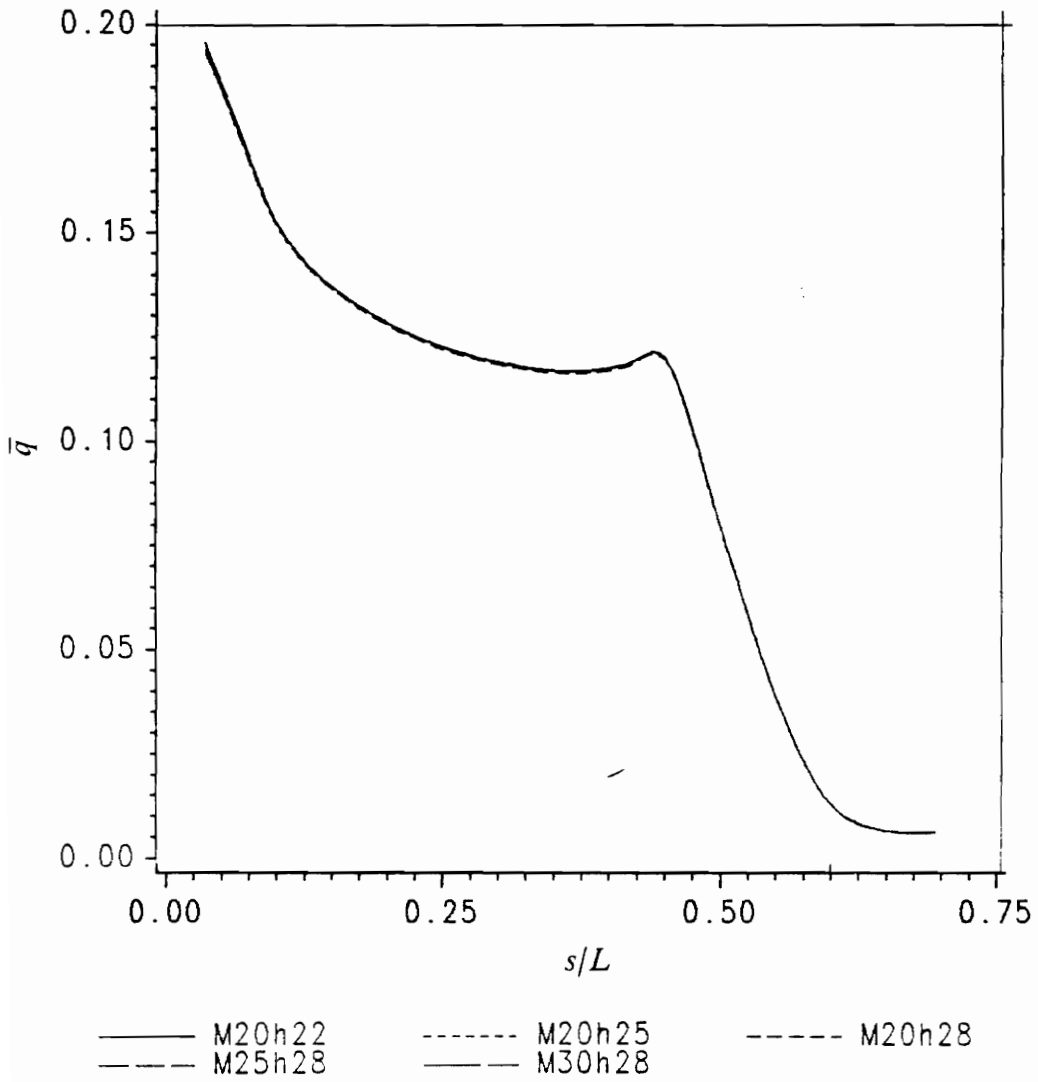


Fig. 26: Non-dimensional heat transfer for spherical cone

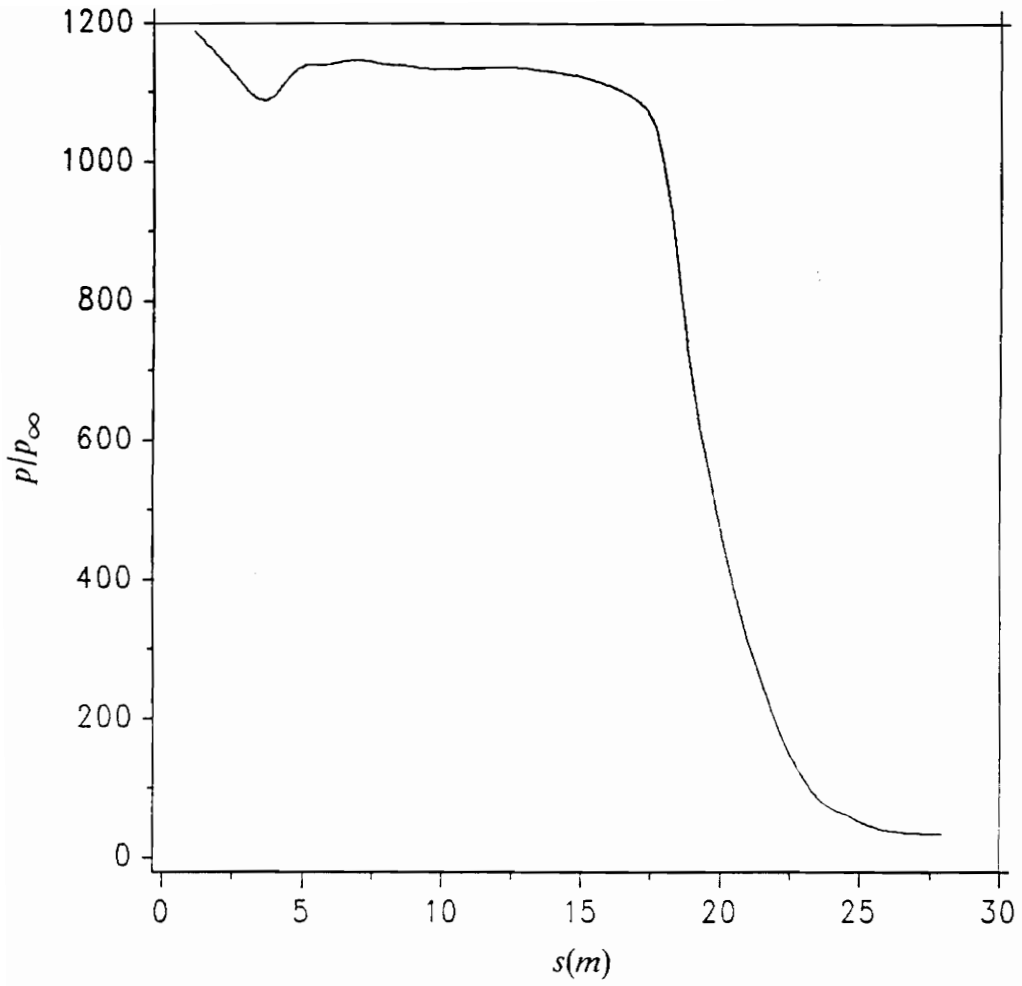


Fig. 27: Boundary layer edge pressure distribution $M_\infty = 20$ (eq. air)

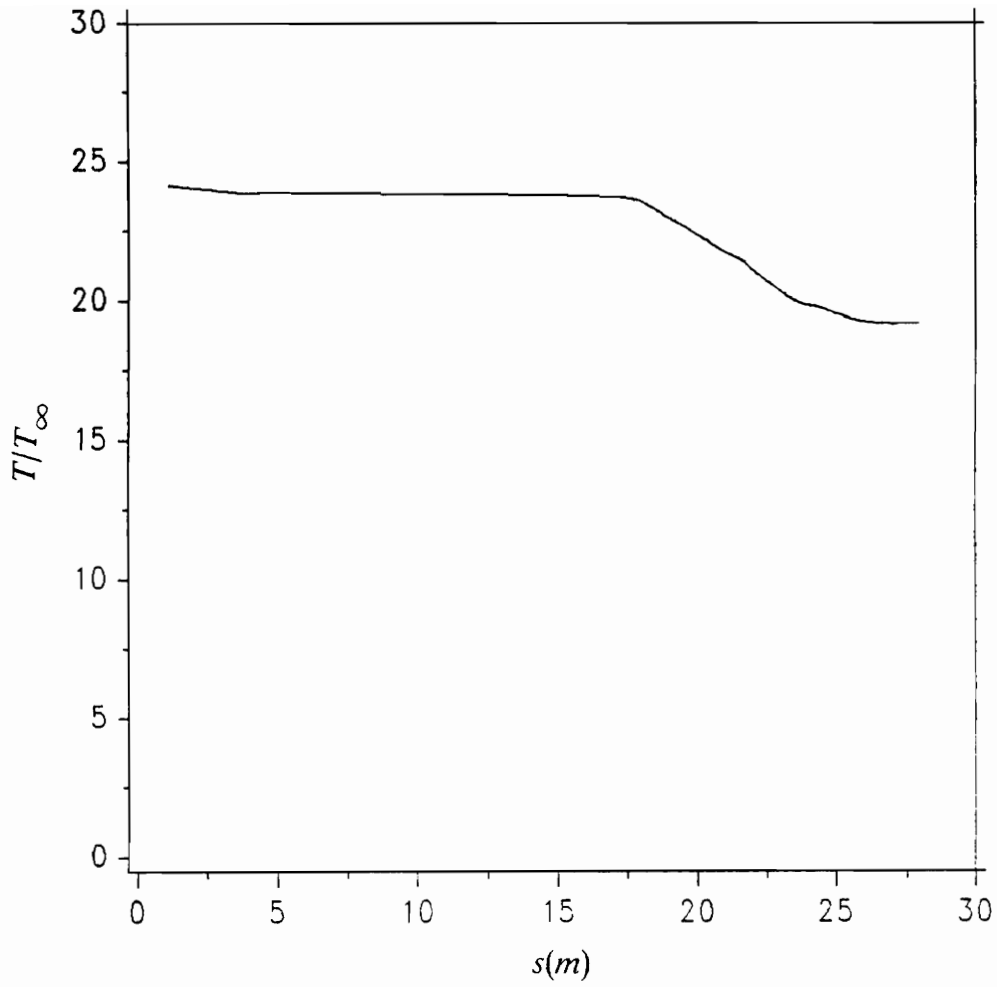


Fig. 28: Boundary layer edge Temperature distribution $M_\infty = 20$ (eq. air)

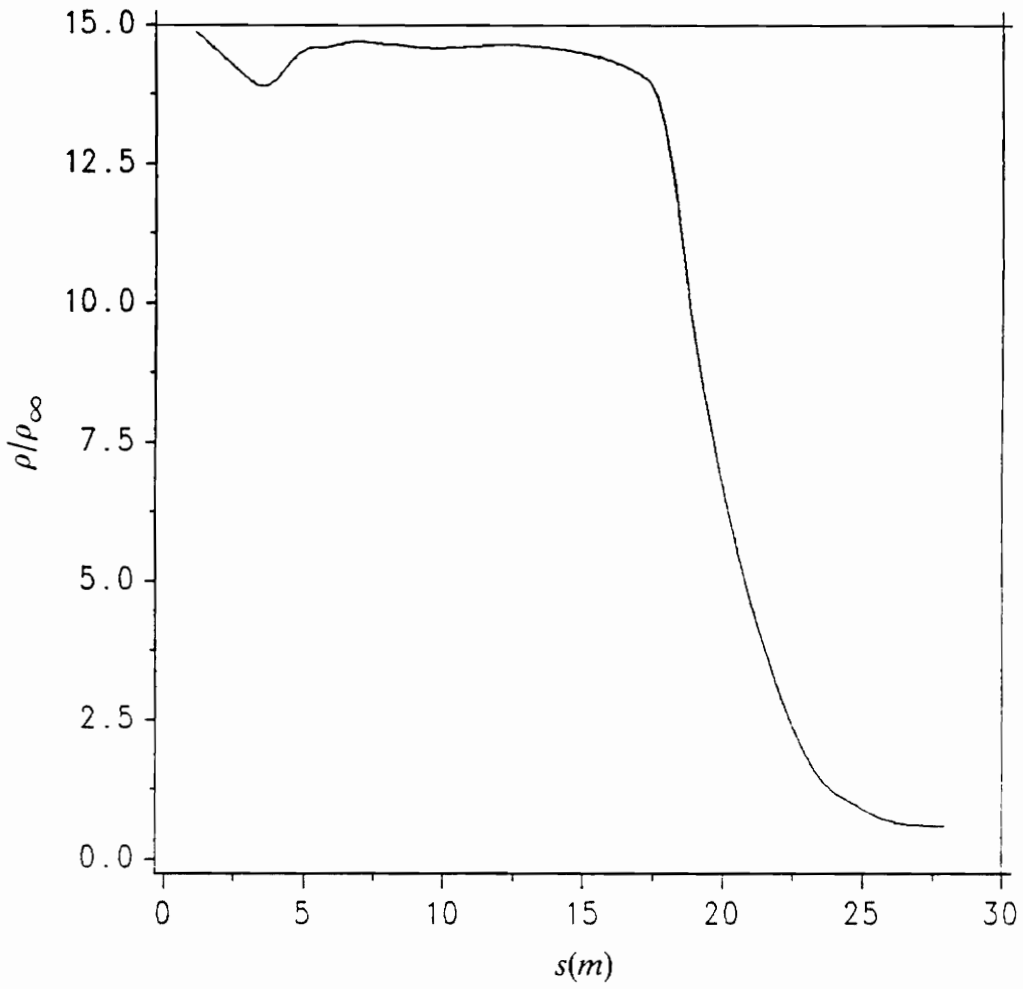


Fig. 29: Boundary layer edge density distribution $M_\infty = 20$ (eq. air)

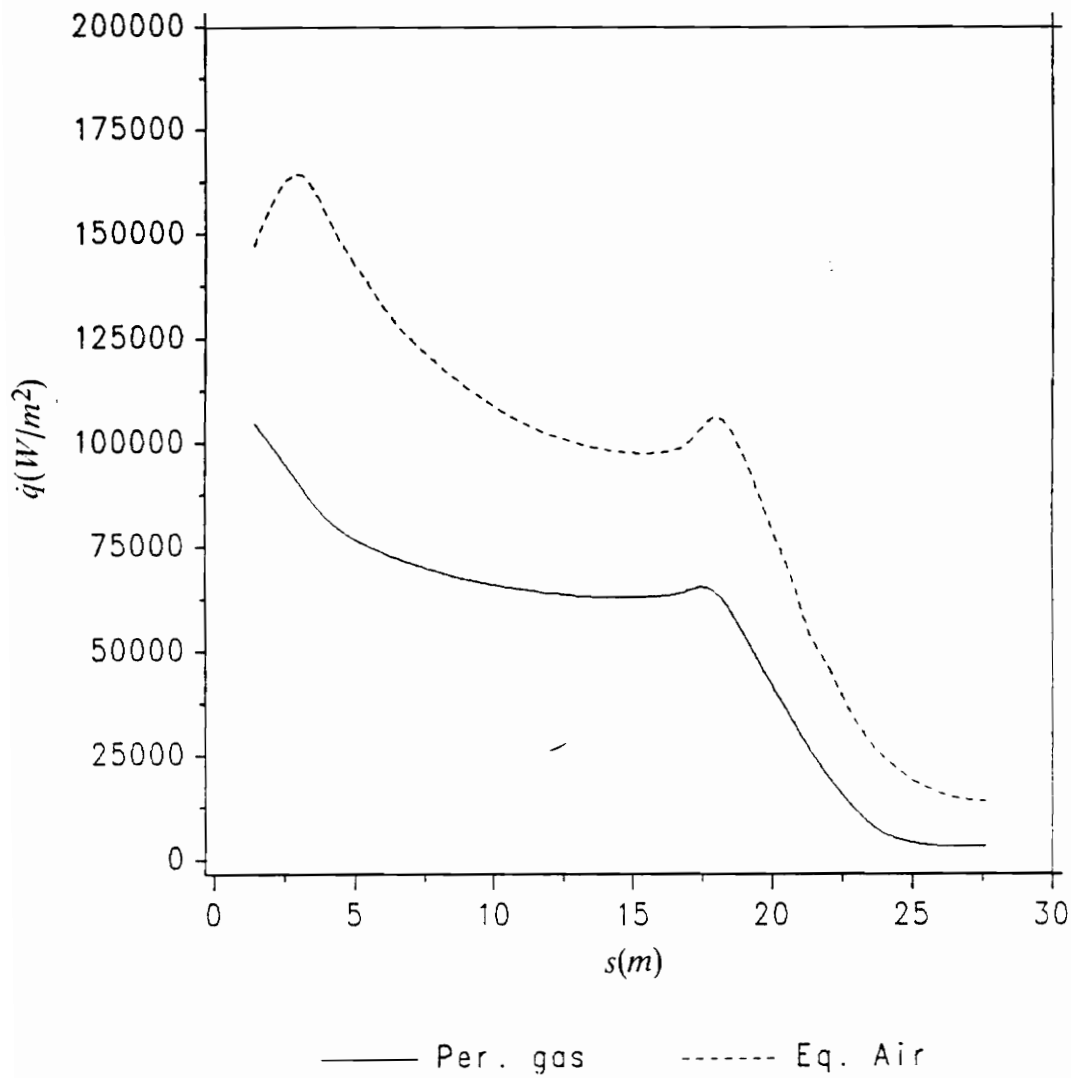


Fig. 30: Comparison of perfect gas and eq. air heating rates

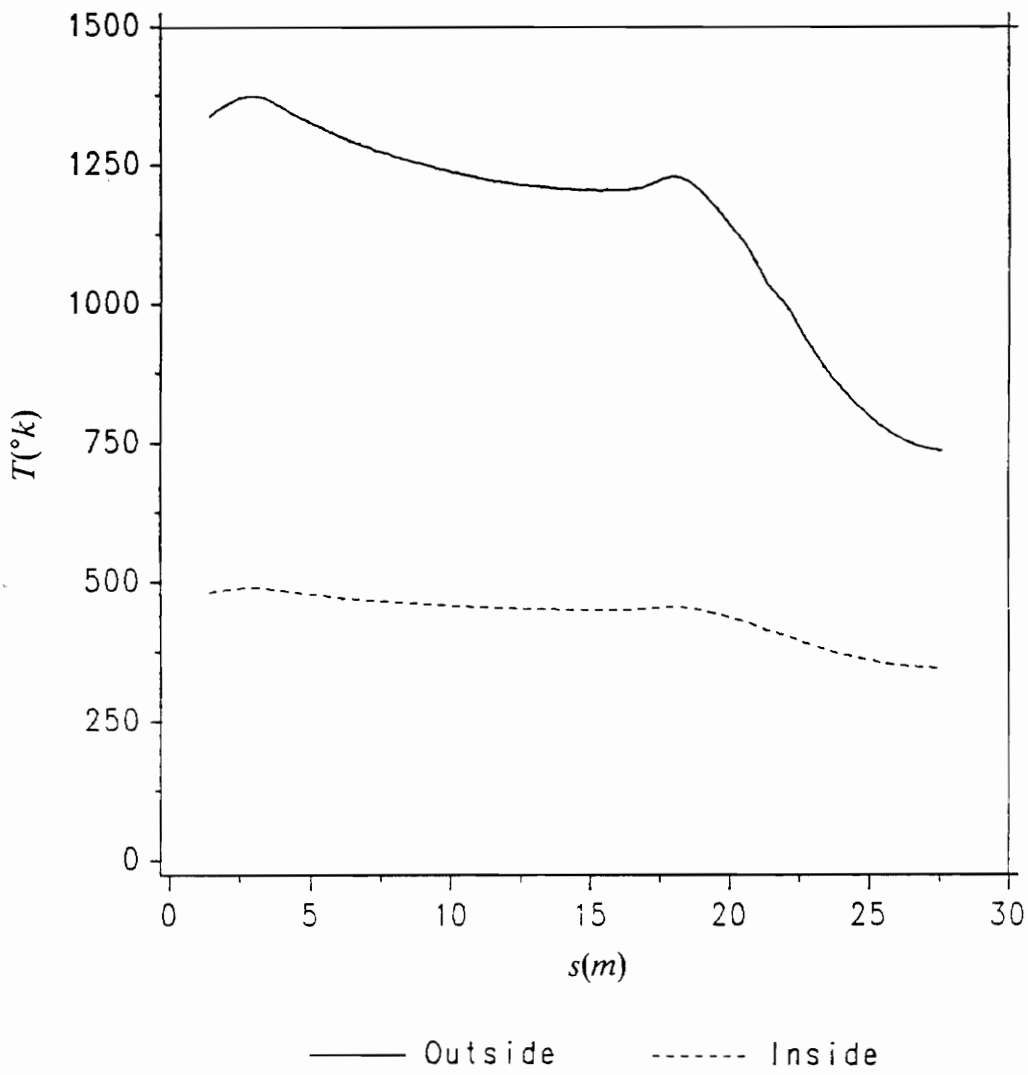


Fig. 31: Wall temperatures $M_\infty = 20$ (eq. air)

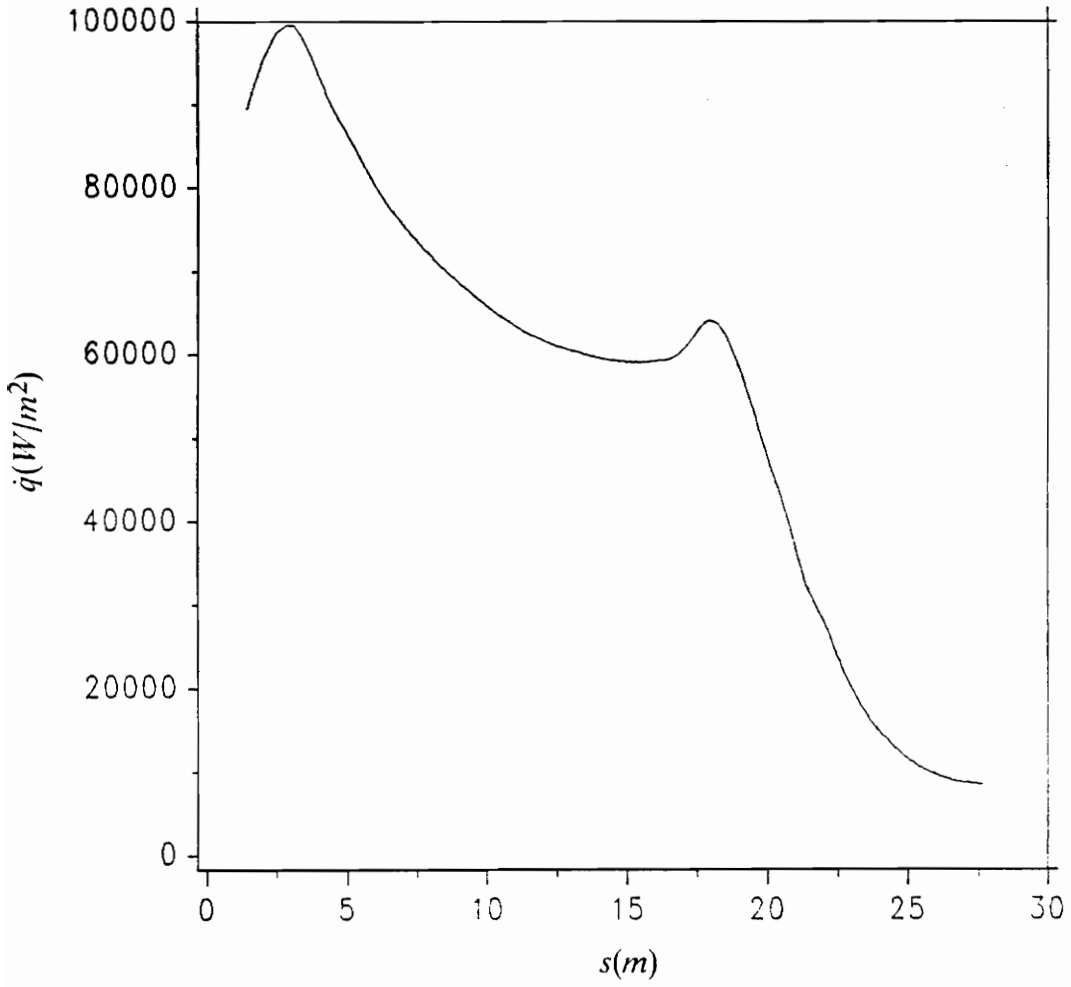


Fig. 32: Heat transfer $M_\infty = 20$, $H = 220$ kft (non-catalytic)

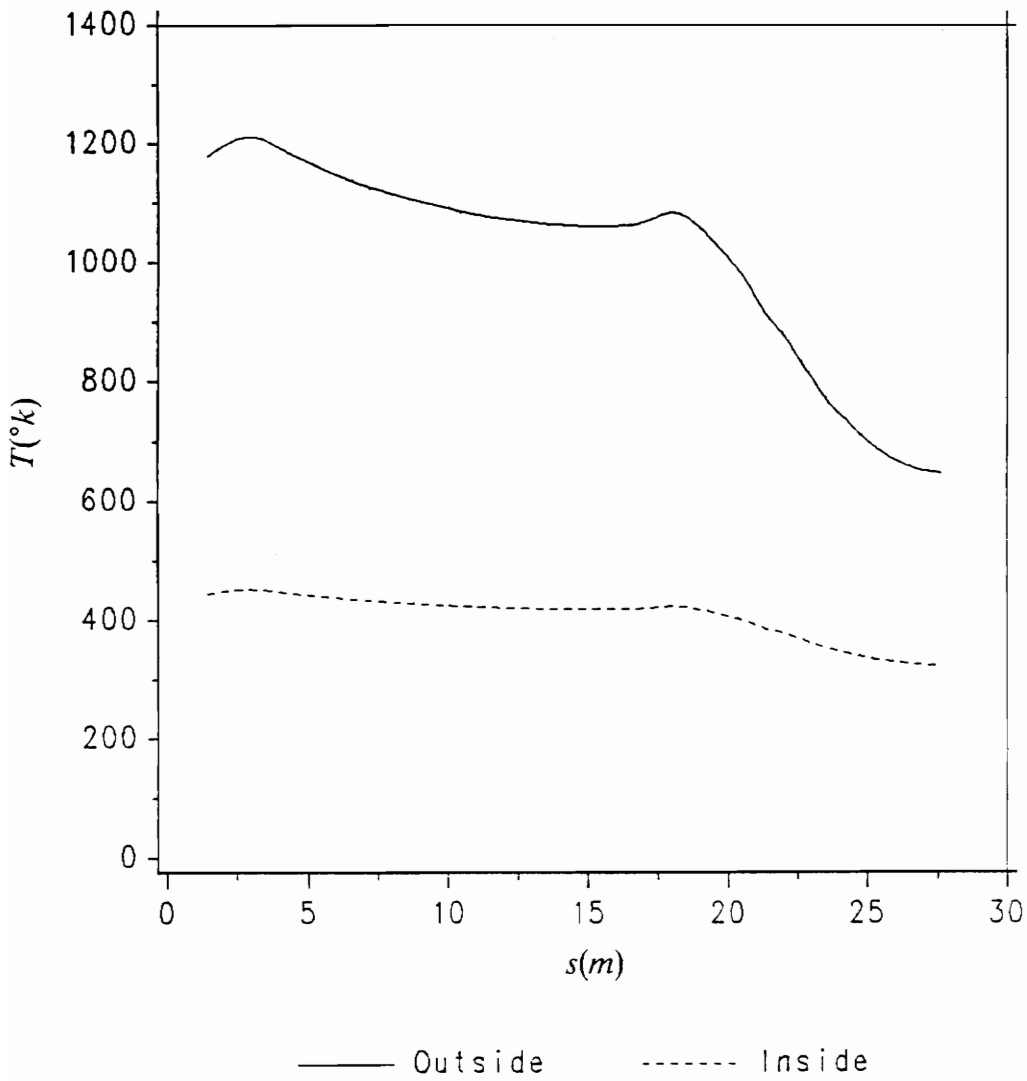


Fig. 33: Wall temperatures $M_\infty = 20$, H = 220 kft (non-catalytic)

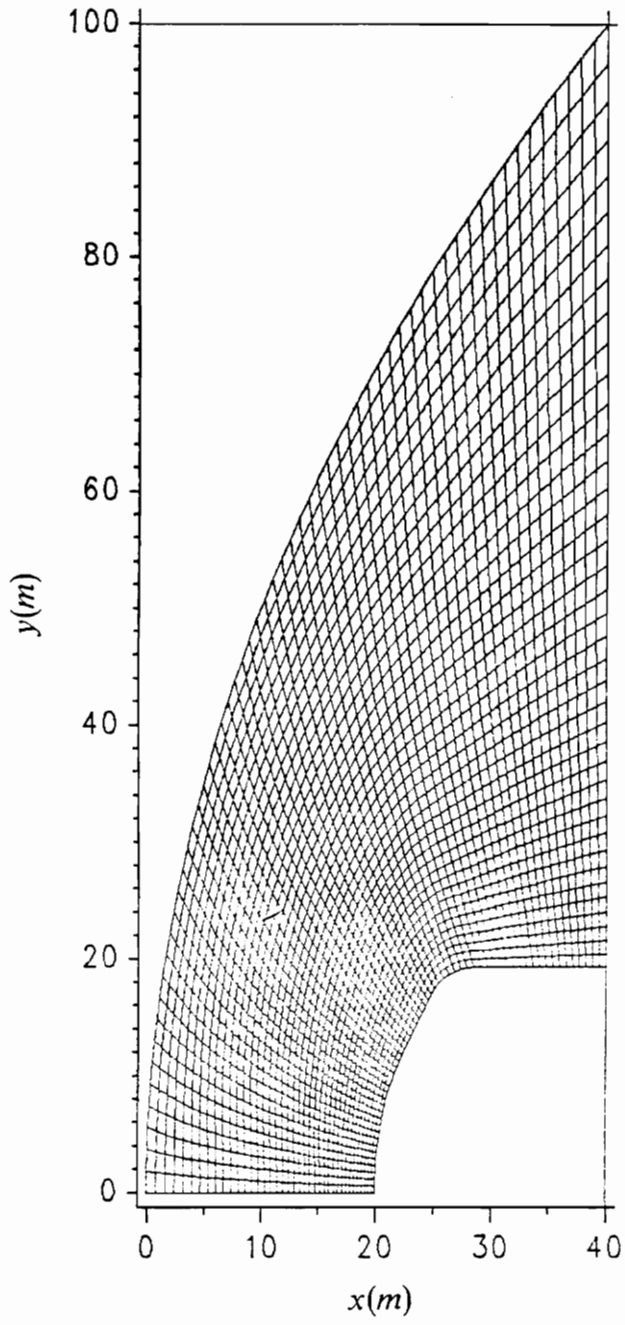


Fig. 34: Computational grid for EBROEC

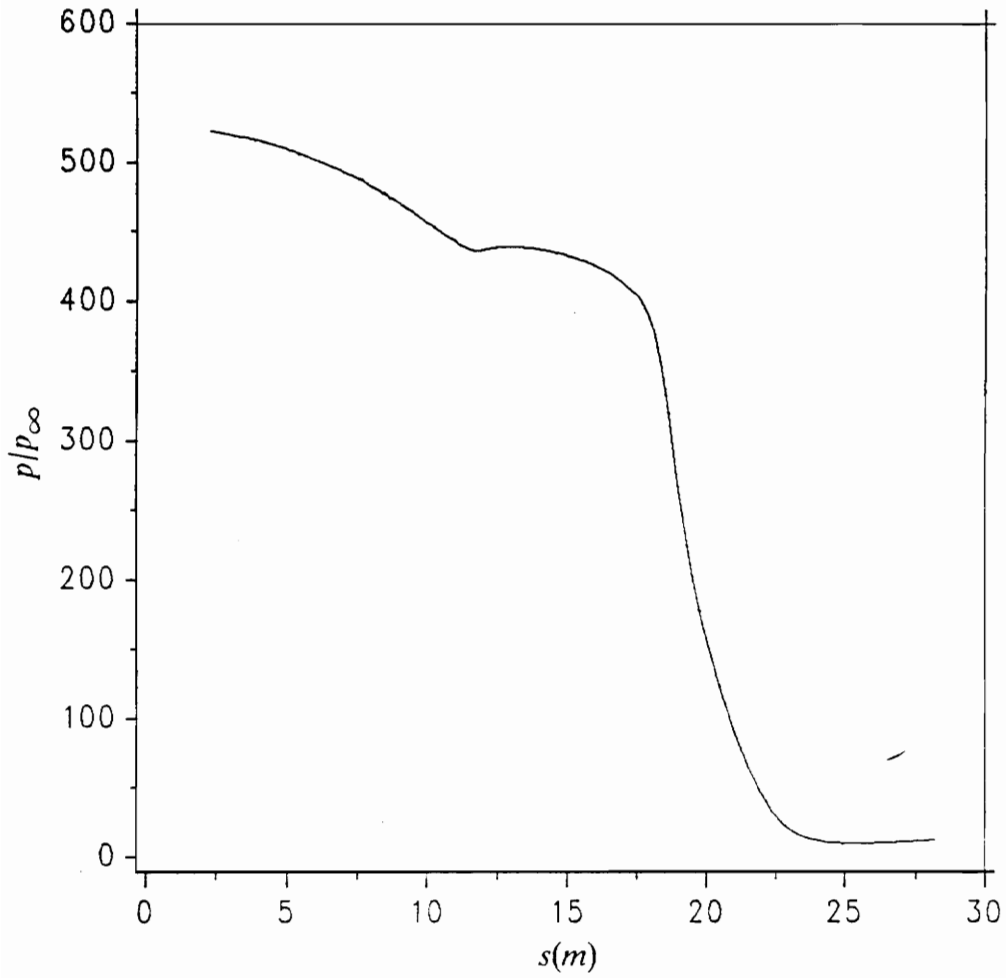


Fig. 35: Boundary layer edge pressure distribution $M_\infty = 20$ (perfect gas)

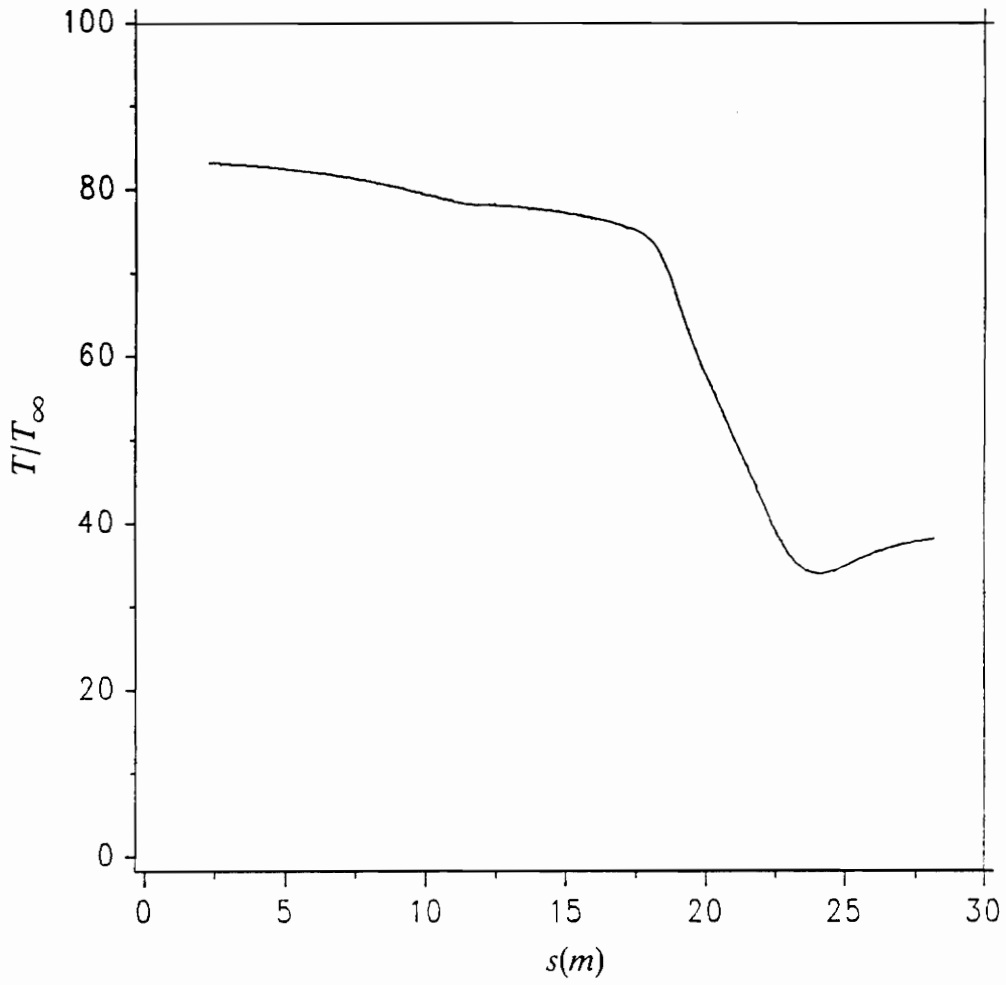


Fig. 36: Boundary layer edge temperature distribution $M_\infty = 20$ (perfect gas)

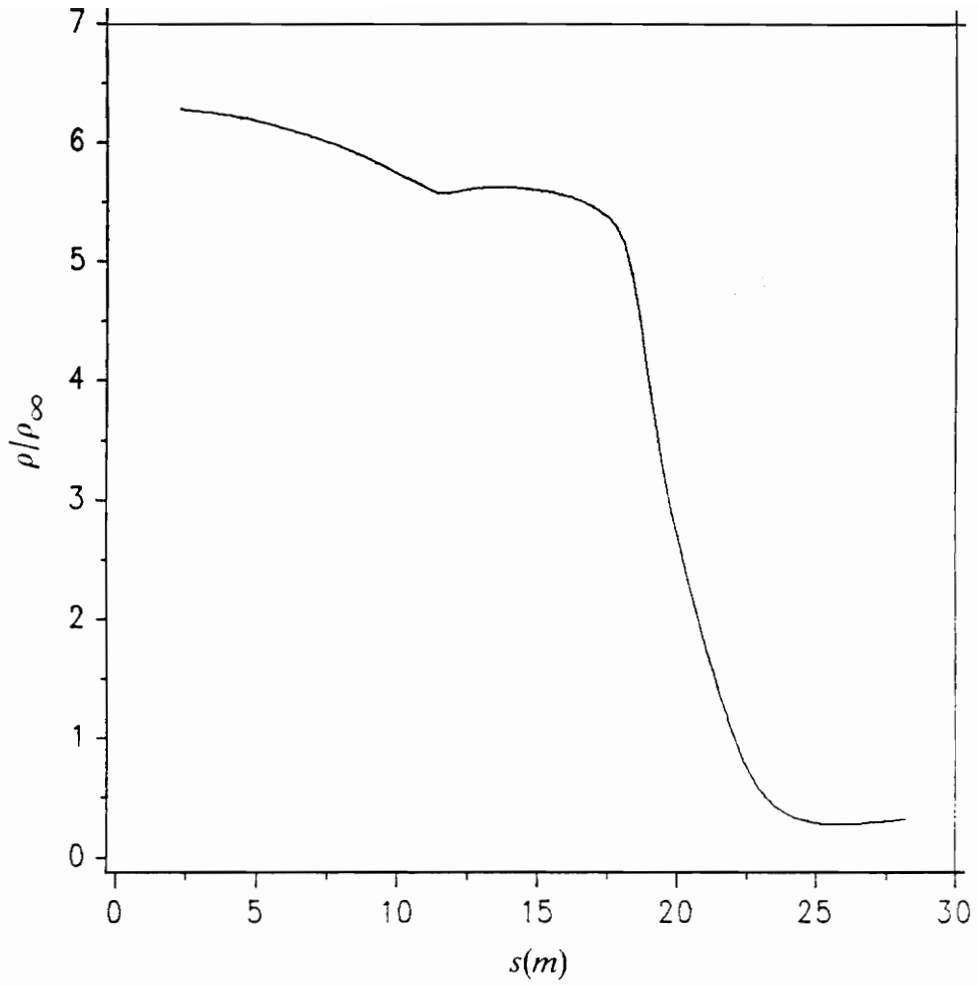


Fig. 37: Boundary layer edge density distribution $M_\infty = 20$ (perfect gas)

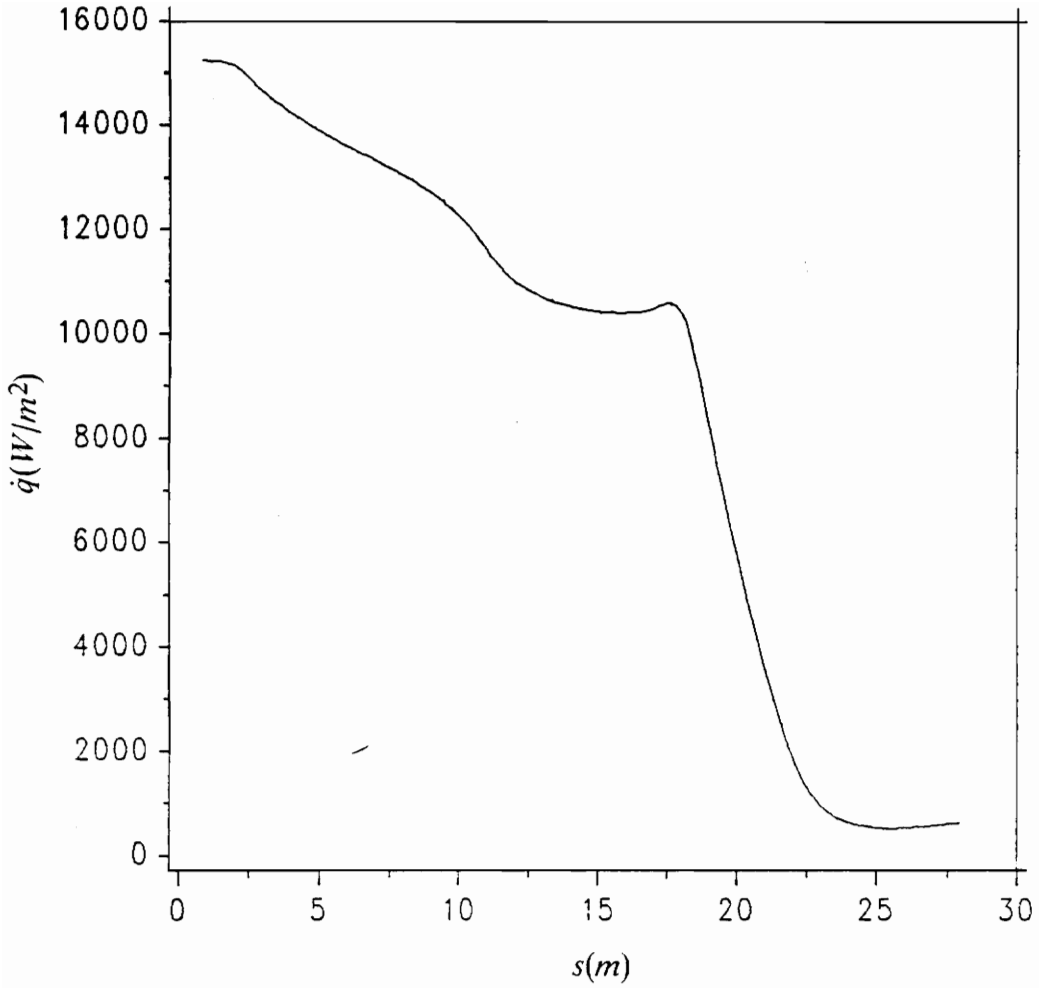


Fig. 38: Heat transfer $M_\infty = 20$, $H = 280$ kft (perfect gas)

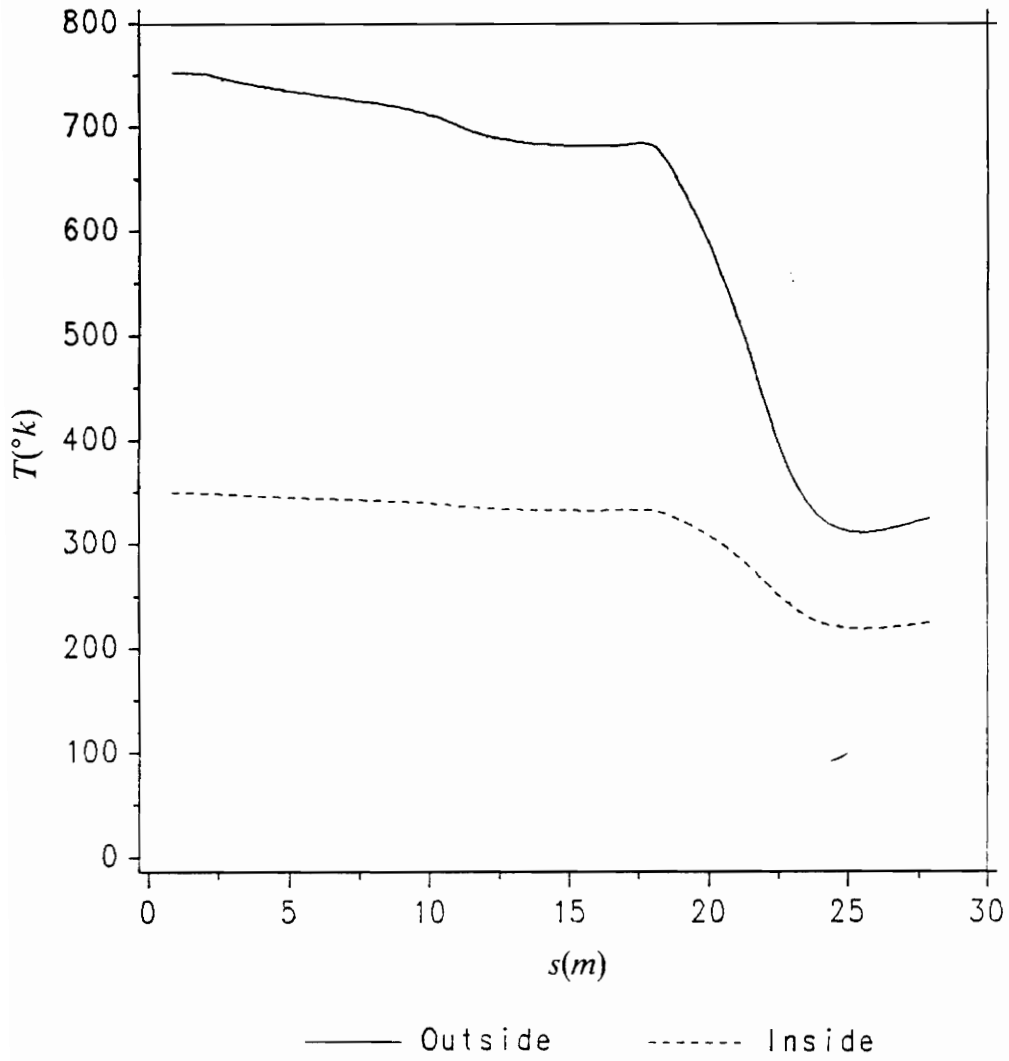


Fig. 39: Wall temperatures $M_{\infty} = 20$, $H = 280$ kft (perfect gas)

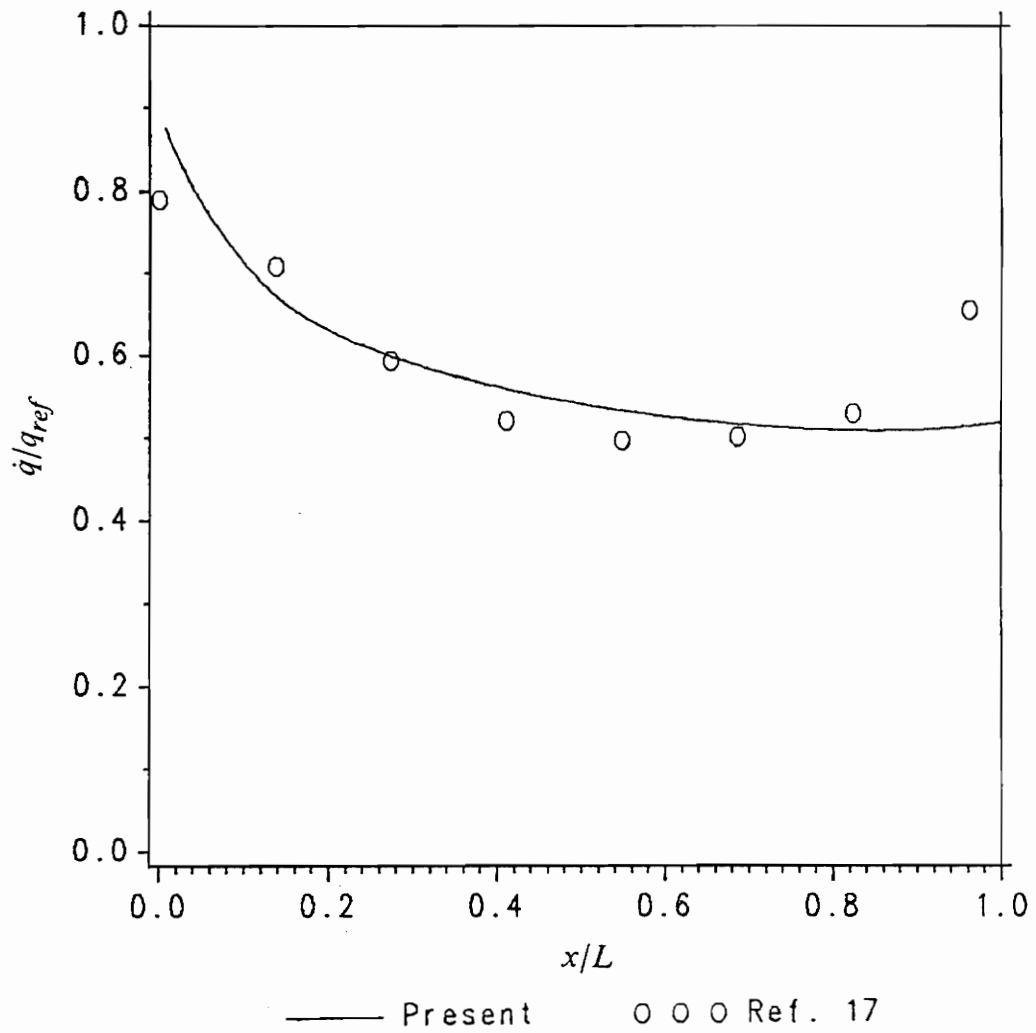


Fig. 40: Comparison of calculated and experimental results for Spherical Cones

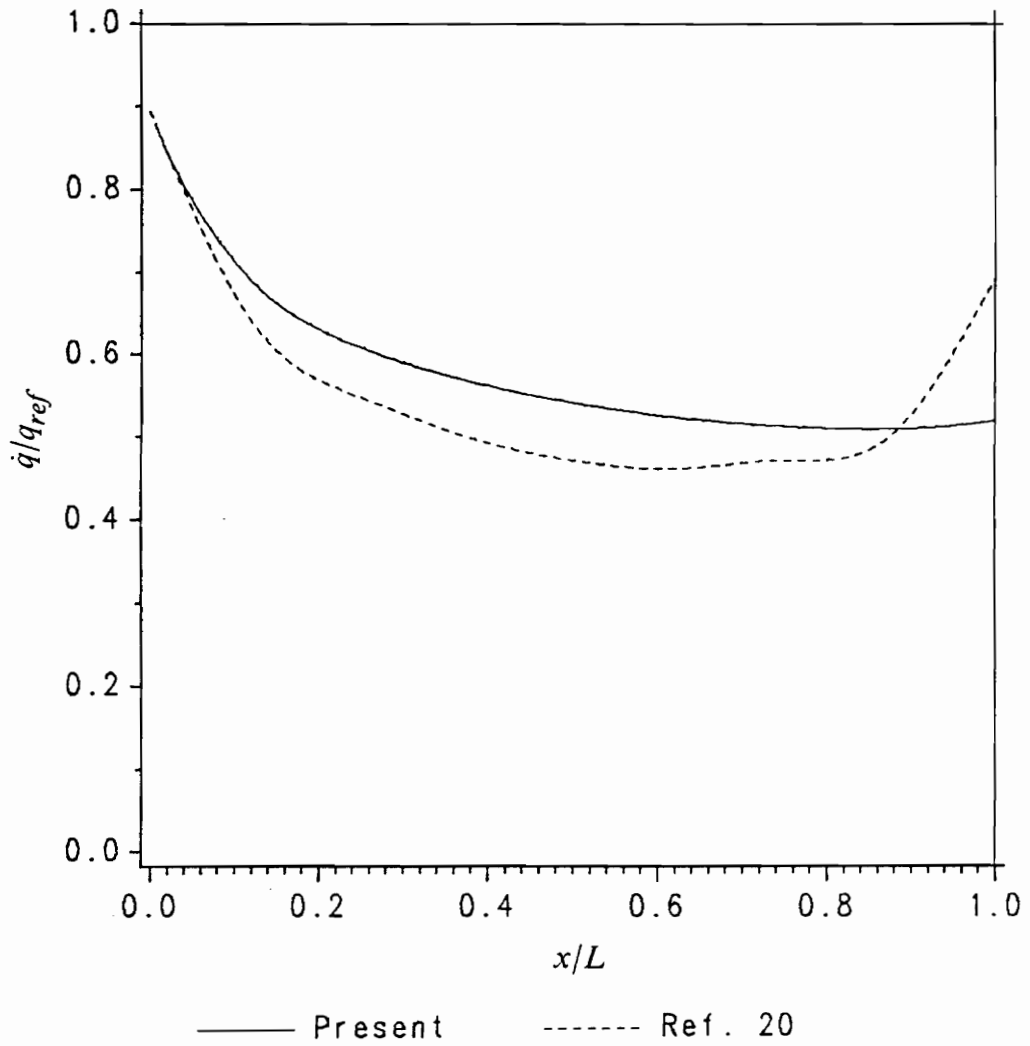


Fig. 41: Comparison of calculated results with other methods for Spherical Cones

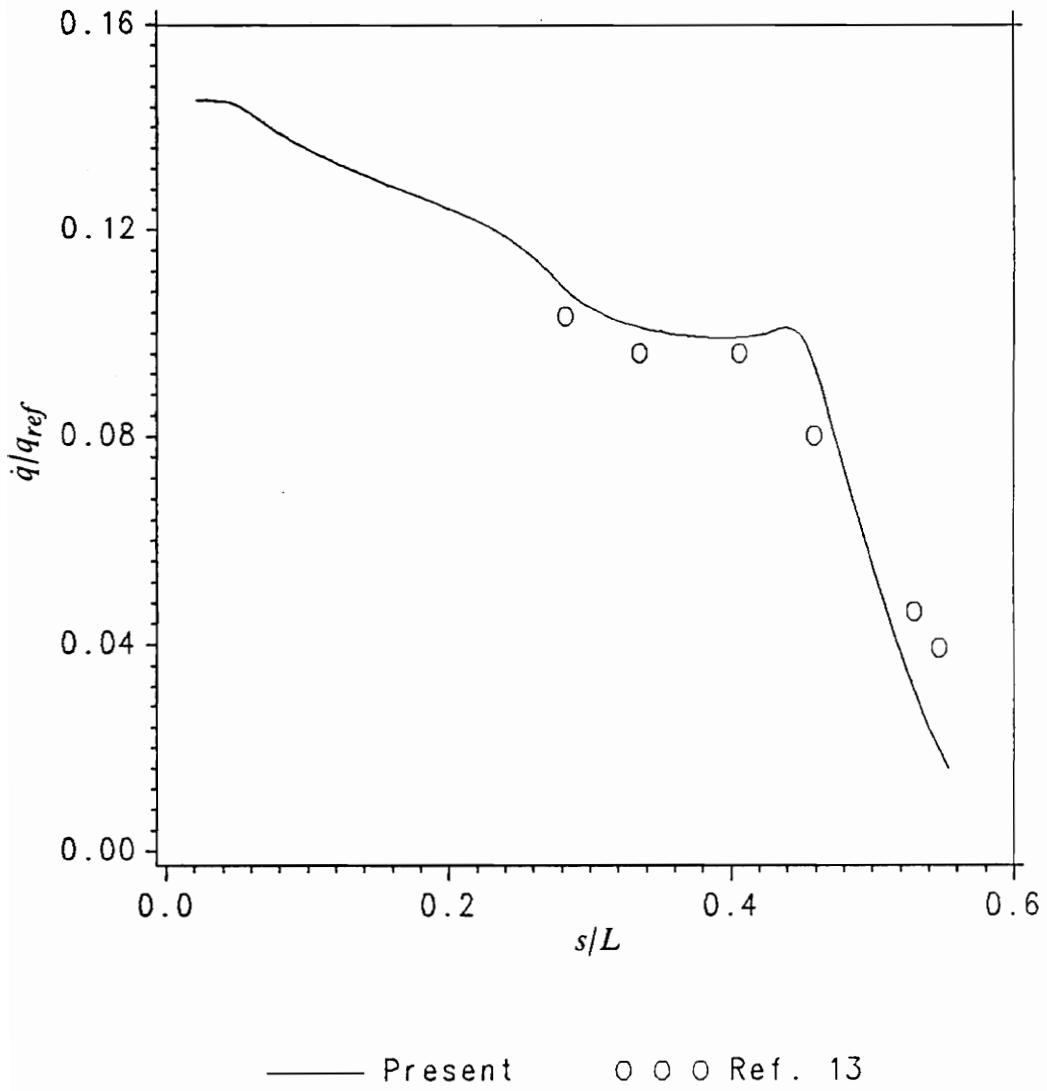


Fig. 42: Comparison of calculated and experimental results for EBROEC

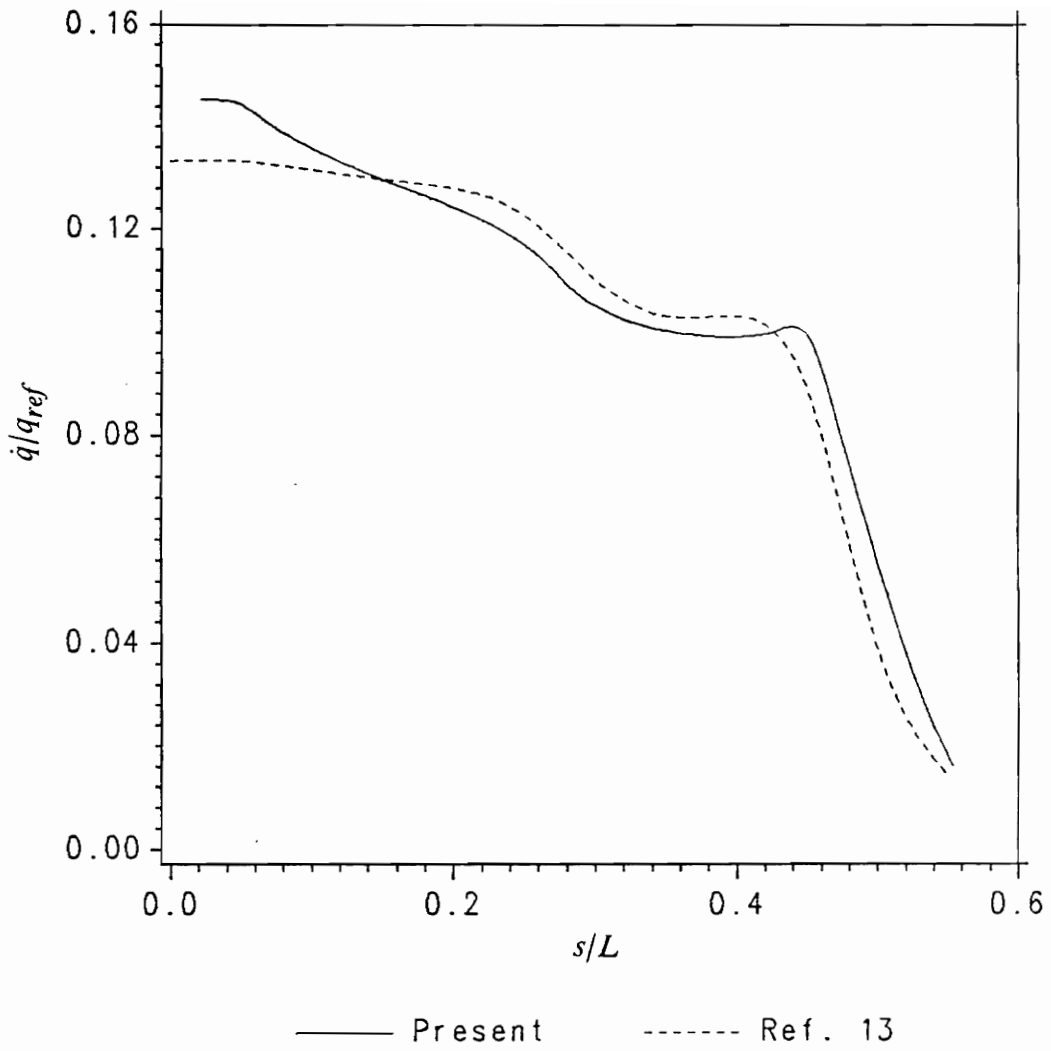


Fig. 43: Comparison of calculated results with other methods for EBROEC

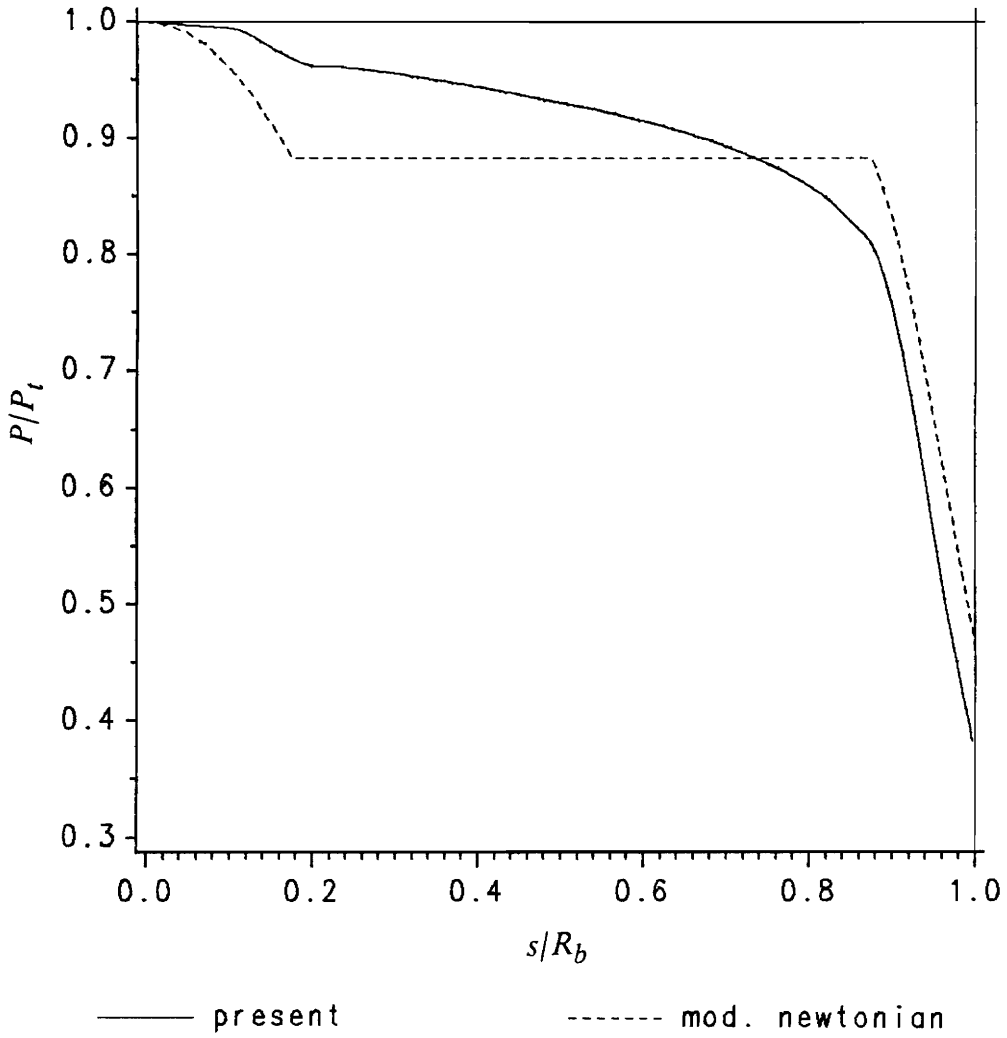


Fig. 44: Pressure distribution predicted by modified Newtonian theory

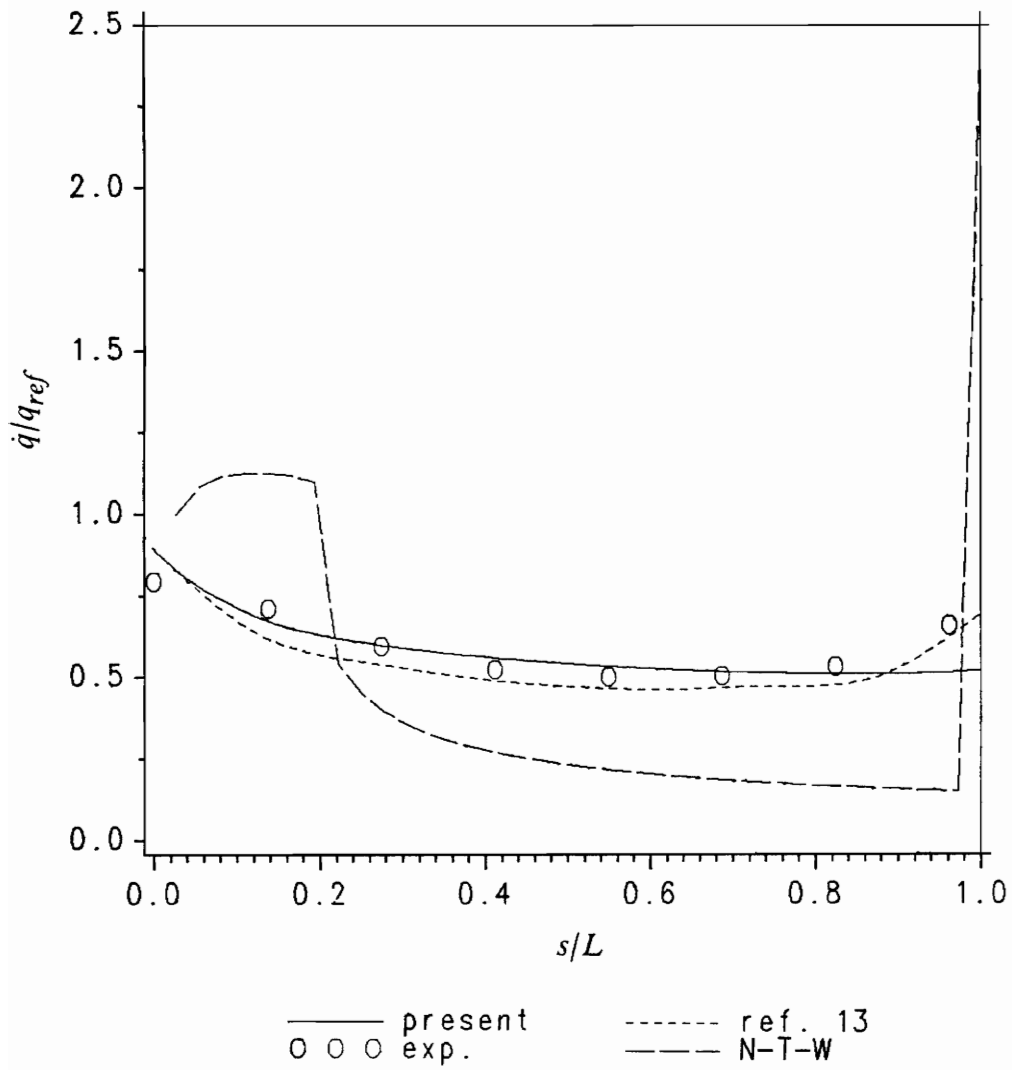


Fig. 45: Heating rates for Newtonian theory with Thwaites-Walz method

Vita

The author was born in Nagpur, India on the third day of February, 1964. He received his Bachelor of Technology degree in Naval Architecture from the Indian Institute of Technology, Kharagpur, India in May, 1985. In January 1986, he joined the Master of Science program in the Aerospace and Ocean Engineering department at Virginia Tech.

